Accepted Manuscript

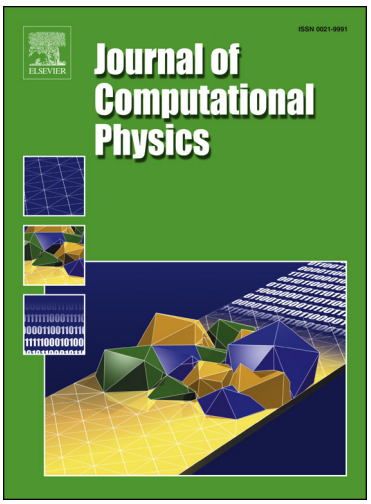

A Flexible Nonlinear Diffusion Acceleration Method for the S_N Transport Equations Discretized with Discontinuous Finite Elements

Sebastian Schunert, Yaqi Wang, Frederick Gleicher, Javier Ortensi, Benjamin Baker et al.

PII: S0021-9991(17)30128-6
DOI: http://dx.doi.org/10.1016/j.jcp.2017.01.070
Reference: YJCPH 7166

To appear in: *Journal of Computational Physics*

Received date: 21 April 2016
Revised date: 8 December 2016
Accepted date: 18 January 2017

Please cite this article in press as: S. Schunert et al., A Flexible Nonlinear Diffusion Acceleration Method for the S_N Transport Equations Discretized with Discontinuous Finite Elements, *J. Comput. Phys.* (2017), http://dx.doi.org/10.1016/j.jcp.2017.01.070

Highlights

- A new flexible nonlinear diffusion acceleration (NDA) method for the first order SN equations is presented.
- The method uses a full diffusion equation discretized with interior penalty discontinuous FEM for acceleration of the SN equations.
- If the SN and diffusion meshes and FEM shape functions are identical the NDA method is unconditionally stable.
- Improvement over CMFD for coarse mesh acceleration is presented for fixed source and eigenvalue problems.

A Flexible Nonlinear Diffusion Acceleration Method for the S_N Transport Equations Discretized with Discontinuous Finite Elements

Sebastian Schunert*, Yaqi Wang, Frederick Gleicher, Javier Ortensi, Benjamin Baker, Vincent Laboure, Congjian Wang, Mark DeHart, Richard Martineau

Nuclear Science and Technology Division, Idaho National Laboratory,
** Corresponding author: 2525 Fremont Avenue, Idaho Falls, ID, 83402,*
sebastian.schunert@inl.gov

Abstract

This work presents a flexible nonlinear diffusion acceleration (NDA) method that discretizes both the S_N transport equation and the diffusion equation using the discontinuous finite element method (DFEM). The method is flexible in that the diffusion equation can be discretized on a coarser mesh with the only restriction that it is nested within the transport mesh and the FEM shape function orders of the two equations can be different. The *consistency* of the transport and diffusion solutions at convergence is defined by using a projection operator mapping the transport into the diffusion FEM space. The diffusion weak form is based on the modified incomplete interior penalty (MIP) diffusion DFEM discretization that is extended by volumetric drift, interior face, and boundary closure terms. In contrast to commonly used coarse mesh finite difference (CMFD) methods, the presented NDA method uses a full FEM discretized diffusion equation for acceleration. Suitable projection and prolongation operators arise naturally from the FEM framework. Via Fourier analysis and numerical experiments for a one-group, fixed source problem the following properties of the NDA method are established for structured quadrilateral meshes: (1) the presented method is unconditionally stable and effective in the presence of mild material heterogeneities if the same mesh and identical shape functions either of the bilinear or biquadratic type are used, (2) the NDA method remains unconditionally stable in the presence of strong heterogeneities, (3) the NDA method with

bilinear elements extends the range of effectiveness and stability by a factor of two when compared to CMFD if a coarser diffusion mesh is selected. In addition, the method is tested for solving the C5G7 multigroup, eigenvalue problem using coarse and fine mesh acceleration. While NDA does not offer an advantage over CMFD for fine mesh acceleration, it reduces the iteration count required for convergence by almost a factor of two in the case of coarse mesh acceleration.

Keywords: Neutron Transport Equation, Nonlinear Diffusion Acceleration, Discontinuous Finite Element Method

1. Introduction

The solution of multiphysics problems in nuclear reactors is an active field of research combining several previously separate disciplines of computational physics. Among the set of physical processes radiation transport takes an important role as the driver for heat production in the nuclear fuel, radiation damage in structural materials, and nuclide transmutation. Therefore, an accurate and efficient radiation transport solver is essential for solving nuclear reactor multiphysics problems. The goal of the Multiphysics Object Oriented Simulation Environment (MOOSE) [1] is the accurate simulation of nuclear reactors requiring a tight coupling of the multiphysics equations, as for example embodied in the simulation efforts of the Transient REActor Test facility (TREAT) [2]. For this purpose, the Rattlesnake application [3] was developed to enable tightly coupled multiphysics transport solutions.

This work focuses on the efficient solution of the first order, multigroup S_N equations arising from the linear Boltzman transport equation after discretization in energy (multigroup) and angle (S_N method) [4]. The first order formulation of the transport equation comprises only first derivative of the angular flux with respect to the independent spatial variables in the streaming term. Iterative convergence of these equations, in their fixed source or eigenvalue form [4], is often very slow for realistic problems and hence acceleration methods are essential. Within this work, we focus on the convergence properties of a new flexible drift-diffusion nonlinear diffusion acceleration (NDA) method for neutron transport problems. NDA was selected because it features a variety of desirable properties: it is inherently effective for solving typically neutron transport problems often cutting the number of transport sweeps (essential unit of computational cost) by a factor of 20-100 and can be applied for both eigenvalue and fixed source problems [5].

Over the course of the last four decades several acceleration methods using the solution of modified diffusion equations have been proposed: Diffusion synthetic acceleration (DSA), [6], [7], [8], Quasi-Diffusion methods (QD), [9], and NDA, [6], [10], [11], [12]. A comprehensive review of acceleration methods can be found in [13]. While DSA is a linear acceleration method, QD and NDA are nonlinear. Moreover, DSA exhibits good performance when applied to the acceleration of fixed source problems, but the extension to eigenvalue problems proves difficult. In constrast, NDA and QD are easily extended to eigenvalue problems and show good performance for their solution.

The most important property of acceleration schemes for the S_N trans-

port equation is the spectral radius ρ defined as the ratio of the iteration error in one iteration divided by the iteration error in the previous iteration. A stable stationary iteration scheme must have a spectral radius ρ smaller than unity, but in practice the more stringent requirement of effectiveness (e.g. $\rho < 0.7$) dictates the range of applicability of an acceleration method. While DSA's spectral radius is bounded by 0.2247 times the scattering radius for the infinite homogeneous medium [13], continuous-in-space mono-energetic slab-geometry transport equation, the same does not necessarily hold true for discretized versions of these equations. Early work on DSA in slab geometry noted that a *consistent* discretization must be selected for ensuring stability and effectiveness of the scheme, [6]. Larsen suggested a four step method for deriving fully consistent discretizations of the diffusion equation from the S_N discretization to achieve unconditional stability [7]. Full consistency implies that the zeroth and first angular moment of the discretized transport equations are used in the acceleration procedure. Later, Adams and Martin, [8], extended this work to discontinuous FEM discretizations using a modified four-step method leading to a partially consistent DSA method where only the zeroth moment of the discretized transport problem is used for acceleration. Reference [8] noted in particular "the most successful schemes have employed diffusion discretizations that are closely related to the transport discretizations being accelerated". In Ref. [14] Warsa uses fully and partially consistent DSA schemes for solving the transport equation on unstructured tetrahedral grids discretized with linear discontinuous FEM. He finds that partially consistent methods' performance can degrade for skewed aspect ratios. Later, Warsa [15] studies the properties of fully and partially consistent DSA methods in the presence of strong material heterogeneities and finds that both performances significantly degrade, thus establishing the importance for testing acceleration methods in strongly heterogeneous problems. Wang developed a partially consistent method based on the modified interior penalty (MIP) scheme. Fourier analysis suggested that method unconditionally stable and mostly effective [16].

Nonlinear diffusion acceleration methods have been proposed as early as [6] with the particular example suggesting to modify the diffusion absorption cross section based on the transport solution to make the diffusion and transport scalar fluxes identical at convergence. However, this work focuses on drift diffusion type NDA methods whose origins can be traced back to the coarse mesh finite difference (CMFD) method suggested by Smith [17], and is commonly referred to as the 2-node CMFD method [10]. This method

has been used both for accelerating nodal diffusion [18] as well as particle transport iterative solutions [19]. CMFD methods set up a simple balance equation incorporating terms evaluated from the high order solution to reproduce surface currents. In this work we refer to NDA methods as a direct extension of CMFD methods in the following sense: instead of using a simple balance, a properly modified diffusion equation that itself is discretized using a finite volume or finite element method is employed for acceleration of the transport problem [12]. To ensure that the transport and diffusion solutions are *consistent*, a volumetric drift vector and additional face and/or boundary terms are added to the discretized diffusion equation. In the particular case of Ref. [12] the SAAF equations discretized with continuous FEM (CFEM) are accelerated using a diffusion equation discretized using CFEM. The diffusion equation encompasses both a volumetric drift term and vacuum boundary terms, but in constrast to DFEM based NDA methods it does not require interior face terms. An example using the CMFD method for accelerating the first order S_N equations is described in [11]. Reference [11] deploys CMFD in conjunction with an inner-outer iteration scheme, i.e. the CMFD equations are set up and solved after a certain number of power iterations.

In Ref. [20] Larsen studies the relationship between DSA and CFMD and finds that the linearized version of the CMFD method is algebraically equivalent to a straight forward extension of the DSA method to coarse meshes (CMDSA). The linearized CMFD and CMDSA methods have nearly identical spectral radii. Wang [3] finds that fine-mesh DSA and NDA methods exhibit similar spectral properties if the optical cell size is sufficiently small, and only mild material heterogeneities are present. Wang [12] also indicated that the linearized spectral radii of the fine-mesh NDA with SAAF CFEM is equal to the one of the DSA in a certain circumstance.

Nonlinear Diffusion Acceleration methods lead to a coupled system of nonlinear equations consisting of the high-order equations and the modified diffusion equations. This system of equations can be solved using fixed point or Picard iterations alternating between solving the transport and diffusion equations [12], [19], or using Newton's method, [5], [21]. While the latter might offer better convergence properties, it is difficult to implement and hence this work focuses on using Picard iteration for obtaining the solution of the NDA system of equations. Ref. [19] concludes that underrelaxation of the Picard iterations in the Smith CMFD formulation is necessary. The NDA method presented within this work does not require underrelaxation for achieving convergence and the Picard iteration is proofed stable both

with Fourier Analysis and numerically.

The NDA method presented in this work is new and differs significantly from previously developed methods. Both the S_N transport equation and the diffusion equation are discretized using discontinuous finite elements (DFEM) of arbitrary and potentially differing order. Additionally, the diffusion equation can be discretized on a coarser mesh with the only restriction being that it is nested within the transport mesh. *Consistency* of the transport and diffusion solutions at convergence is defined by using a projection operator mapping the transport FEM space into the diffusion FEM space that is rigoriusly derived from the FEM weak forms. The diffusion weak form is based on the incomplete MIP diffusion DFEM discretization [16] that is extended by volumetric drift, face closure, and boundary closure terms. In contrast to the NDA method in [12], this work focuses on the first order S_N equations and the associated diffusion equation discretized with DFEM, and supporting both differing FEM spaces and coarse mesh acceleration. Compared to standard CMFD methods, the region of stability of the presented NDA method can be extended to larger optical cell sizes and cell aspect ratios; and under certain conditions the presented NDA method is unconditionally stable [22], [23]. Compared to the improved 2-node CMFD method in Ref. [19] that successfully applies an ad-hoc linear prolongation technique, this work is consistently defined within a potentially higher order FEM framework; within this FEM framework projection and prolongation operators naturally associated with the employed FEM spaces are readily available. Finally, our NDA method uses an additive update that by design does not add spurious information, i.e. information that is not strictly contained in the diffusion FEM representation, to the transport solution as opposed to the commonly used multiplicative update of the transport system. Finally, similar to Lee's work [11] this work focuses on the first order S_N equations. However, there are two significant differences between Lee's and this work: (1) Lee only utilizes CMFD, i.e. a simple balance, and not NDA, and (2) CMFD is applied in an inner-outer iteration scheme focusing on the transport solves and using CMFD as an occasional correction. In contrast, the NDA method described in this work uses occasional transport updates moving most of the work into the diffusion system.

In section 2 the weak forms of the multigroup eigenvalue S_N equations and the diffusion problem are introduced. Then, projection and prolongation operators are presented enabling a rigorous definition of *consistency* of the transport and diffusion solutions. This is followed by the introduction of

a suitable drift term, face closures, and boundary closure into the diffusion weak form.The NDA algorithm is described in section 3. Section 4 presents a Fourier analysis of the investigated NDA method for a single, quadrilateral element with periodic boundary conditions. In section 5, numerical results are presented for a one-group, fixed source test problem and in section 6 numerical results for the C5G7 test problem are presented. We do not measure the efficiency of the presented NDA method based on its CPU times because we currently do not have an efficient transport sweeper for inverting the streaming plus collision operator; the number of transport sweeps can indicate the efficiency because the transport sweeps take the largest fraction of the CPU times in practical applications with sufficiently fine angular quadrature. The work is summarized and conclusions are drawn in section 7. In sections 5 and 6 we compare the performance of NDA and CMFD algorithms. It is understood, that CMFD in this context simply translates into using constant shape functions for discretizing the diffusion system. The difference to the traditional CMFD algorithm is the additive update of the transport system as opposed to the normal scaling approach.

2. Consistent Weak Forms of the S_N and Diffusion Equations

In this section, the weak forms of the multigroup diffusion and S_N transport equations are derived. The presented NDA method uses the diffusion system for accelerating the iterative solution of the S_N transport equation. However, diffusion and transport solutions are not identical even when obtained on the same mesh and using the same FEM bases. Therefore, appropriate closure terms are introduced in the diffusion equation such that the solution of the S_N equations is *consistent* to the diffusion solution at convergence. It is understood that the solutions are *consistent* only at convergence and therefore "at convergence" is omitted for the remainder of this work. The definition of *consistency* in the general case where diffusion and transport solutions are obtained on different meshes and/or using different FEM bases will be provided in section 2.3. To increase clarity of the notation, quantities associated with the transport system are denoted by upper case symbols, while diffusion quantities use lower case symbols: for example the scalar flux in the transport system is denoted by Φ, but the scalar flux in the diffusion system is denoted by ϕ. The exception to this rule are the diffusion coefficient and the volumetric drift vector that are customarily denoted by capital letters.

2.1. Weak Form of the S_N Equations

This work focuses on the acceleration of the steady-state, multigroup, first order, S_N equations. The eigenvalue form of the S_N euqations for direction $\vec{\Omega}_m$ is given by:

$$\vec{\Omega}_m \cdot \nabla \Psi_{g,m} + \Sigma_{t,g}(\vec{r})\Psi_{g,m}(\vec{r}) = \frac{1}{4\pi}\sum_{g'=1}^{G} \Sigma_s^{g'\to g}\Phi_{g'} + \frac{K_g(\vec{r})}{4\pi k}\sum_{g'=1}^{G} \nu\Sigma_{f,g'}(\vec{r})\Phi_{g'}(\vec{r}), \text{ on } \mathcal{D}, \tag{1}$$

$$\Psi_{g,m} = 0 \text{ on } \partial\mathcal{D}^s : \vec{n}\cdot\vec{\Omega}_m < 0, \tag{2}$$

$$\Psi_{g,m} = \Psi_{g,m^r} \text{ on } \partial\mathcal{D}^r : \vec{n}\cdot\vec{\Omega}_m < 0, \tag{3}$$

where g is the group index, G is the total number of energy groups, $\vec{\Omega}_m$ is the m-th angular direction, $\Psi_{g,m}$ is the angular flux and Φ_g is the scalar flux

evaluated with the angular quadrature $\{\vec{\Omega}_m, w_m, m = 1, .., M\}$:

$$\Phi_g = \sum_{m=1}^{M} w_m \Psi_{g,m}, \tag{4}$$

$\mathcal{D}$ is the spatial domain, $\partial\mathcal{D}^s$ and $\partial\mathcal{D}^r$ are the fixed inflow and reflective boundaries, respectively, $\vec{n}$ is an outward normal vector on the boundary, m_r is the reflected direction associated with $\vec{\Omega}_m$ that is assumed to be also present in the angular quadrature set, $\Sigma_{t,g}$ is total interaction cross section in group g, $\Sigma_s^{g'\to g}$ is the scattering transfer cross section from group g' to group g, K_g is the fission spectrum, $\nu\Sigma_{f,g}$ is the fission neutron production cross section, and k is the multiplication factor that is an unknown in Eq. 1. While there exist multiple eigenvalues and associated flux distributions satisfying Eq. 1, only the largest eigenvalue achieves a positive, self-sustaining flux distribution. This largest eigenvalue is referred to as multiplication value and the flux distribution is referred to as fundamental mode. When solving the equation with an external source, k will be fixed to one. The eigenvalue problem can be rewritten by setting the multiplication factor equal to the total number of neutrons produced by fission essentially eliminating the eigenvalue from Eq. 1. In this form, the eigenvalue problem can be viewed as a nonlinear problem with the solution normalized to k. We intentionally use the capitalized notation for cross sections in Eq. 1 to distinguish the S_N cross sections from the diffusion system cross sections and focused on isotropic scattering throughout this work. Even though we do not consider anisotropic scattering we believe the described NDA method can be applied to problems with moderate anisotropy (averaged scattering cosine less than 0.5) as suggested in [24].

To obtain the weak form we multiply Eq. 1 with an arbitrary test function $\Psi^*_{g,m}$, integrate over the domain $\mathcal{D}$, sum over all angular directions, and finally apply Green's identity:

$$B\left(\Psi, \Psi^*\right) - R\left(\Psi, \Psi^*\right) - S\left(\Psi, \Psi^*\right) = \frac{1}{k} F\left(\Psi, \Psi^*\right), \tag{5}$$

with the bilinear forms being defined as:

$$
\begin{aligned}
B\left(\Psi,\Psi^{*}\right) &= \sum_{g=1}^{G}\sum_{m=1}^{M} w_m \left(\left(\Psi_{g,m},\left(-\vec{\Omega}_m\cdot\nabla+\Sigma_{t,g}\right)\Psi^{*}_{g,m}\right)_{\mathcal{D}} - \left\langle \Psi^{-}_{g,m},[\![\Psi^{*}_{g,m}]\!]\right\rangle_{\Gamma}\right)\\
R\left(\Psi,\Psi^{*}\right) &= \sum_{g=1}^{G}\sum_{E\in\partial D^r}\sum_{\vec{\Omega}\cdot\vec{n}>0} w_m \left\langle \Psi_{g,m},\Psi^{*}_{g,m^r}\right\rangle_{E}\\
S\left(\Psi,\Psi^{*}\right) &= \frac{1}{4\pi}\sum_{g=1}^{G}\sum_{g'=1}^{G}\left(Q_{s,g',g},\Phi^{*}_{g}\right)_{\mathcal{D}}\\
F\left(\Psi,\Psi^{*}\right) &= \frac{1}{4\pi}\sum_{g=1}^{G}\sum_{g'=1}^{G}\left(Q_{f,g',g},\Phi^{*}_{g}\right)_{\mathcal{D}},
\end{aligned}
\tag{6}
$$

where $\Phi^{*}_{g}=\sum_{m=1}^{M} w_m\Psi^{*}_{g,m}$, E is an FEM element's face, $\vec{n}$ is an arbitrarily oriented normal vector on E (outward normal vector on $\partial\mathcal{D}$), f^{+} and f^{-} are downwind and upwind values of f, respectively, Γ is the set of all interior faces, $[\![f]\!]=f^{+}-f^{-}$ is the jump across an element's face with the upwind and downwind sides being defined by $\vec{\Omega}_m$, and

$$
\left(f,g\right)_{\mathcal{D}} = \int_{\mathcal{D}} dV\, fg \tag{7}
$$

$$
\left\langle f,g\right\rangle_{E} = \int_{E} dA\left|\vec{\Omega}_m\cdot\vec{n}\right| fg. \tag{8}
$$

In Eq. 5, the scattering and fission sources $Q_{s,g',g}$ and $Q_{f,g',g}$ are defined for convenience when defining the NDA system of equations. For the unaccelerated S_N equations, Eq. 1, they are given by $Q_{s,g',g}=\Sigma_s^{g'\to g}\Phi_{g'}$ and $Q_{f,g',g}=K_g\nu\Sigma_{f,g'}\Phi_{g'}$. For convenience the lumped source Q_g is defined as:

$$
Q_g=\frac{1}{4\pi}\sum_{g'=1}^{G}Q_{s,g',g}+\frac{1}{4\pi k}\sum_{g'=1}^{G}Q_{f,g',g}. \tag{9}
$$

2.2. Weak Form of the Incomplete Interior Penalty Diffusion Equation

The continuous multi-group diffusion equation with vacuum Robin boundary conditions and reflective boundary conditions on $\mathcal{D}^s$ and $\mathcal{D}^r$, respectively,

is given by:

$$
\begin{aligned}
-\vec{\nabla} D_p \cdot \vec{\nabla}\phi_p + \sigma_{r,p}\phi_p &= \sum_{p' \neq p} \sigma_s^{p' \to p}\phi_{p'} + \frac{\chi_p}{k}\sum_{p'=1}^{P} \nu\sigma_{f,p'}\phi_{p'}, \\
\frac{\phi_p}{4} + \frac{D_p}{2}\vec{n}\cdot\vec{\nabla}\phi_p &= 0 \text{ on } \partial\mathcal{D}^s, \\
\vec{n}\cdot\vec{\nabla}\phi_p &= 0 \text{ on } \partial\mathcal{D}^r,
\end{aligned} \tag{10}
$$

where p is the coarse group index, P is the total number of coarse energy groups, D_p is the diffusion coefficient, $\sigma_{r,p}$ is the removal cross section, χ_p is the fission spectrum, and $\sigma_{f,p'}$ is the fission neutron production cross section. The corresponding weak form of the multi-group diffusion equation discretized with the incomplete interior penalty (IP) discontinuous FEM method [16] is given by:

$$
b\left(\phi, \phi^*\right) = \frac{1}{k} f\left(\phi, \phi^*\right), \tag{11}
$$

with

$$
\begin{aligned}
b\left(\phi, \phi^*\right) = &\sum_{p=1}^{P} \left(D_p\vec{\nabla}\phi_p, \vec{\nabla}\phi_p^*\right)_{\mathcal{D}} + \sum_{p=1}^{P} \left(\sigma_{r,p}\phi_p, \phi_p^*\right)_{\mathcal{D}} \\
&- \sum_{p=1}^{P}\sum_{p' \neq p} \left(\sigma_s^{p' \to p}\phi_{p'}, \phi_p^*\right)_{\mathcal{D}} + \sum_{p=1}^{P} \left(\{\!\{D_p\vec{\nabla}\phi_p \cdot \vec{n}\}\!\}, [\![\phi_p^*]\!]\right)_{\Gamma} \\
&+ \sum_{p=1}^{P} \left(\kappa_p [\![\phi_p]\!], [\![\phi_p^*]\!]\right)_{\Gamma} + \sum_{p=1}^{P} \left(\frac{\phi_p}{2}, \phi_p^*\right)_{\mathcal{D}^s} \\
f\left(\phi, \phi^*\right) = &\sum_{p=1}^{P}\sum_{p'=1}^{P} \left(\chi_p \nu\sigma_{f,p'}\phi_{p'}, \phi_p^*\right)_{\mathcal{D}}
\end{aligned} \tag{12}
$$

where κ_p is the stabilization parameter, $[\![f]\!] = f^+ - f^-$ is the jump across an element's face with the upwind and downwind side being defined by the face's normal vector (normal vector $\vec{n}$ points from $-$ to $+$), $\{\!\{f\}\!\} = \frac{1}{2}(f^+ + f^-)$. It is noted that the orientation of the face normal vectors is irrelevant.

The stabilization parameter κ_p is chosen as the modified interior penalty

(MIP) coefficient defined in [16]:

$$\begin{aligned} \kappa_p &= \max(\kappa_p^{IP}, \frac{1}{4}) \\ \kappa_p^{IP} &= \begin{cases} \frac{1}{\frac{h^+}{D_p^+}+\frac{h^-}{D_p^-}}, & q = 0; \\ 2p^2\left(\frac{D_p^+}{h^+}+\frac{D_p^-}{h^-}\right), & \text{else.} \end{cases} \end{aligned} \tag{13}$$

where $q = 0, 1, ...$ is the order of the FEM basis functions used for discretizing the diffusion equation, and $h^{\pm}$ is a measure of the mesh spacing associated with the current element's face defined as the distance of the face centroid $\vec{r}_F$ and the element's centroid $\vec{r}_C$ projected along the normal $\vec{n}$:

$$h = \left|\vec{n} \cdot (\vec{r}_C - \vec{r}_F)\right|. \tag{14}$$

The MIP formulation ensures that the penalty is large enough for optically thick cells. In section 4, a Fourier analysis demonstrates that the IP penalty can lead to an unstable NDA method on coarse mesh cells.

2.3. The Consistent Diffusion Weak Form

The solutions of Eq. 5 and 11, Φ_g and ϕ_p, respectively, are different even if both equations are discretized on the same mesh and with the same FEM basis. To make Φ_g and ϕ_p *consistent*, volume, face, and boundary closure terms are added to the diffusion equation Eq. 11. These closure terms are discussed in section 2.3.2. Before derivation of the closure terms, the definition of *consistency* of diffusion and S_N solution is discussed in section 2.3.1.

2.3.1. Projection and Prolongation Operators

The projection operator $\Pi[\cdot]$ mapping a member of the S_N FEM space to the diffusion FEM space is introduced in order to define the meaning of *consistency* of Φ_g and ϕ_p that are potentially defined within different FEM spaces. Using the projection operator, Φ_g and ϕ_p are *consistent* if:

$$\phi_p = \Pi[\Phi_g]. \tag{15}$$

Within the FEM framework, an explicit representation of the projection operator can obtained by requiring that

$$\left(\phi_p^*, \Phi_g\right)_{\mathcal{D}} = \sum_{g \in p} \left(\phi_p^*, \phi_p\right)_{\mathcal{D}}. \tag{16}$$

Let us denote the set of FEM basis functions by $\{b\}_{k=1}^{K}$ and $\{B\}_{t=1}^{T}$ for the diffusion and S_N system, respectively, and collect them in the vectors $\vec{b}$ and $\vec{B}$. Then Eq. 16 can be recast as:

$$\left(\vec{b},\vec{b}\right)_{\mathcal{D}}\vec{\phi_p} = \sum_{g\in p}\left(\vec{b},\vec{B}\right)_{\mathcal{D}}\vec{\Phi}_g, \tag{17}$$

where $\vec{\phi_p}$ and $\vec{\Phi}_g$ are the expansion coefficients of ϕ_p and Φ_g, respectively. Note, that $\left(\vec{b},\vec{b}\right)_{\mathcal{D}}$ is simply the diffusion mass matrix and hence is invertible.

The reverse operation of the projection is referred to as prolongation and is denoted by $\Pi^{-1}[\cdot]$. It maps a member of the diffusion FEM space to the S_N FEM space. The prolongation operator is defined equivalently to Eq. 16:

$$\left(\Phi_g^*,\Phi_g\right)_{\mathcal{D}} = \left(\Phi_g^*,\phi_p\right)_{\mathcal{D}}. \tag{18}$$

Totally equivalently to Eq. 17, an explicit representation is given by:

$$\left(\vec{B},\vec{B}\right)_{\mathcal{D}}\vec{\Phi}_g = \left(\vec{B},\vec{b}\right)_{\mathcal{D}}\vec{\phi_p}. \tag{19}$$

Within the remainder of this work, we assume that the diffusion FEM space is a subset of the S_N FEM space. This is typically true because the diffusion equation is typically solved on a coarser mesh and either using the same FEM basis or a lower order FEM basis.

2.3.2. Closure Terms

In this section, closure terms are introduced into the diffusion weak form to make its solution *consistent* with the solution of the transport equation. For deriving the closure terms, we subsitute an isotropic test function Φ^* into Eq. 5. The resulting equation is referred to as the angular balance of the transport weak form and is given by:

$$B\left(\Psi,\Phi^*\right) - S\left(Q_s,\Phi^*\right) = \frac{1}{k}F\left(Q_f,\Phi^*\right), \tag{20}$$

where:

$$\begin{aligned} B\left(\Psi,\Phi^*\right) = \sum_{g=1}^{G}\Big\{&-\left(\vec{J}_g,\nabla\Phi_g^*\right) + \left(\Sigma_{t,g}\Phi_g,\Phi_g^*\right) + \left(\left[\!\left[J_g^{out}\right]\!\right],\left[\!\left[\Phi_g^*\right]\!\right]\right)_{\Gamma} \\ &+ \left(J_g^{out},\Phi_g^*\right)_{\mathcal{D}^s}\Big\}. \end{aligned} \tag{21}$$

In Eq. 21 the current $\vec{J}$ is given by:

$$\vec{J}_g = \sum_{m=1}^{M} w_m \vec{\Omega}_m \Psi_{g,m}, \tag{22}$$

and the partial outflow current J_g^{out} is defined as:

$$\begin{aligned} J_g^{out,\pm} &= \sum_{\pm(\vec{\Omega}\cdot\vec{n})<0} w_m \left|\vec{\Omega}_m \cdot \vec{n}\right| \Psi_m^{\pm}. \\ J_g^{out} &= J_g^{out,-}. \end{aligned} \tag{23}$$

In order to satisfy Eq. 15 at convergence, we modify the diffusion weak form Eq. 11 by adding closure terms and defining the diffusion cross sections. The modifications are straight forward to derive by comparing Eq. 20 with the diffusion weak form. The consistent NDA diffusion weak form is given by:

$$b\left[\Psi\right](\phi,\phi^*) + c\left[\Psi\right](\phi,\phi^*) = \frac{1}{k} f\left[\Psi\right](\phi,\phi^*), \tag{24}$$

where the notation $a\left[\cdot\right](\cdot,\cdot)$ denotes that the *consistent* diffusion bilinear forms[1] depend on the high order solution. The closure term $c\left[\Psi\right](\phi,\phi^*)$ is given by:

$$c\left[\Psi\right](\phi,\phi^*) = \sum_{p=1}^{P} \left(\widehat{D}_p\phi_p, \vec{\nabla}\phi_p^*\right)_{\mathcal{D}} + \sum_{p=1}^{P} \left(\left[\!\left[\widehat{\kappa}_p\phi_p\right]\!\right], \left[\!\left[\phi_p^*\right]\!\right]\right)_{\Gamma} + \sum_{p=1}^{P} \left(\frac{\alpha_p}{4}\phi_p, \phi_p^*\right)_{\mathcal{D}^s}, \tag{25}$$

[1]The forms are still bilinear if Ψ is taken to be fixed.

where the following quantities are obtained from the S_N cross sections via flux weighting:

$$\text{Removal cross sections } \sigma_{r,p} = \frac{\Pi\left[\left(\Sigma_{t,g} - \Sigma_s^{g\to g}\right)\Phi_g\right]}{\Pi\left[\Phi_g\right]}$$

$$\text{Scattering cross section } \sigma_s^{p'\to p} = \frac{\Pi\left[\left(\sum_{g\in p}\Sigma_s^{g'\to g}\right)\Phi_{g'}\right]}{\Pi\left[\Phi_{g'}\right]}$$

$$\text{Fission production cross section } \nu\sigma_{f,p'} = \frac{\Pi\left[\nu\Sigma_{f,g'}\Phi_{g'}\right]}{\Pi\left[\Phi_{g'}\right]}$$

$$\text{Fission spectrum } \chi_p = \frac{\Pi\left[K_g\left(\sum_{g'}\nu\Sigma_{f,g'}\Phi_{g'}\right)\right]}{\Pi\left[\left(\sum_{g'}\nu\Sigma_{f,g'}\Phi_{g'}\right)\right]}.$$

If the low order space is piece-wise constant, these formulations reduce to the conventional homogenized flux-weighted cross sections. The diffusion coefficient D_p is defined as:

$$D_p = \frac{\Pi\left[\frac{1}{3\Sigma_{t,g}}\Phi_g\right]}{\Pi\left[\Phi_g\right]}. \tag{26}$$

Furthermore, $\widehat{D}_p$ is the drift vector, $\hat{\kappa}$ is the face closure, and α is the fixed source boundary coefficient. The drift vector is computed by:

$$\widehat{D}_p = -\frac{D_p\nabla\Pi\left[\Phi_g\right] + \Pi\left[\vec{J}\right]}{\Pi\left[\Phi_g\right]}, \tag{27}$$

At convergence the term comprising D_p in the drift vector, Eq. 27, cancels the corresponding term in the diffusion weak form, Eq. 24, regardless of the definition of D_p itself. Therefore, D_p does not influence consistency, but it does influence the spectral properties of the NDA algorithm described in section 3. The diffusion coefficient is essentially a free parameter in the described NDA algorithm. We do not have any conclusive evidence on which choice of the diffusion coefficient would yield the smallest spectral radius. However, in [25] we found that using non-local tensor diffusion coefficients

for the periodical horizontal interface problem improves the spectral radius significantly when compared to the definition used in this work. The fixed source boundary coefficient α is given by:

$$\alpha_p = 4\frac{\Pi\left[J_g^{out,-}\right]}{\Pi\left[\Phi_g\right]} - 2, \tag{28}$$

For the definition of the face closure, two distinct definitions are considered in this work both of which lead to consistency in the sense of Eq. 15, but differ in their spectral properties. The two variations are referred to as the SYW and pNDA method and are based on the SYW and PCMFD methods in Ref. [26]. The particular formulations are different from [26] as this work focuses on first order S_N methods discretized with DFEM. The SYW and pNDA closures are given by:

$$\begin{aligned}
\text{SYW: } \hat{\kappa}_p^{\pm} &= \frac{\Pi\left[J_g^{out,\pm}\right]}{\Pi\left[\Phi_g^{\pm}\right]} \pm D_p \frac{\vec{n}\cdot\nabla\Pi\left[\Phi_g^{\pm}\right]}{2\Pi\left[\Phi_g^{\pm}\right]} - \kappa_p \\
\text{pNDA: } \hat{\kappa}_p^{\pm} &= \frac{\Pi\left[J_g^{out,\pm}\right] + \frac{\phi_s}{4} \mp \left[\!\left[\frac{1}{2}\kappa_p\phi_p - \frac{1}{4}D_p\left(\vec{n}\cdot\nabla\Pi\left[\Phi_g\right]\right)\right]\!\right]}{\Pi\left[\Phi_g^{\pm}\right]}.
\end{aligned} \tag{29}$$

For the pNDA closure, the face scalar flux ϕ_s is defined by:

$$\phi_{s,g} = \frac{\left\{\!\!\left\{\Pi\left[\Phi_g\right]\widehat{D}_p/h\right\}\!\!\right\}}{\left\{\!\!\left\{\widehat{D}_p/h\right\}\!\!\right\}} \tag{30}$$

Using Eqs. 24 through 30 leads to a *consistent* diffusion weak form in the sense of Eq. 15. This can be proved by subsituting an angularly isotropic test function into Eq. 5 to obtain the angular balance. When converged, the resulting angular balance and Eq. 24 are identical.

From a homogenization perspective, the low-order diffusion weak form can be understood as a formalism on how a homogenized low-order representation can retain all features of the high-order transport solution that can be represented on a coarser mesh, using a lower order FEM basis and fewer energy groups.

3. Nonlinear Diffusion Acceleration Algorithm

In section 2, consistent weak forms of the S_N and diffusion equations, Eq. 5 and 24, respectively, have been derived. These equations are consistent in the sense that when the angular flux is known and the cross sections and the closure terms are constructed, the computed scalar fluxes ϕ_p satisfy Eq. 15. In this section, the nonlinear diffusion acceleration algorithm that is used for the effective iterative solution of Eq. 5 is presented.

In other words, when an estimate of the solution of the high order transport system is given, we can solve the low order diffusion system to obtain the eigenvalue and the scalar flux in the lower dimensional space, which can be used in the scattering and fission terms for evaluating the residual of the transport system. We can view this as a non-linear problem, or we can break this non-linear system into two pieces by using the following Picard iteration:

$$b\left[\Psi^l\right]\left(\phi^{l+1/2},\phi^*\right)+c\left[\Psi^l\right]\left(\phi^{l+1/2},\phi^*\right)=\frac{1}{k^{l+1/2}}f\left[\Psi^l\right]\left(\phi^{l+1/2},\phi^*\right), \tag{31}$$

$$\begin{aligned} B\left(\Psi^{l+1},\Psi^*\right)-R\left(\Psi^l,\Psi^*\right)-S\left(Q_s^{l+1/2},\Phi^*\right)&=\frac{1}{k^{l+1/2}}F\left(Q_f^{l+1/2},\Phi^*\right)\\ Q_{s,g',g}^{l+1/2}&=\Sigma_s^{g'\to g}\Phi_{g'}^{p,l+1/2}\\ Q_{f,g',g}^{l+1/2}&=K_g\nu\Sigma_{f,g'}\Phi_{g'}^{p,l+1/2}. \end{aligned} \tag{32}$$

The index l denotes the iteration index in the fixed point solution method utilized for the solution of the NDA system of equations and will be discussed shortly. One distinct feature of the presented NDA method is the prolongation of the diffusion scalar flux ϕ_p to the S_N weak form denoted by $\Phi_g^{p,l+1/2}$ in Eq. 32. The prolonged scalar flux is computed by:

$$\Phi_g^{p,l+1/2}=\Phi_g^l+\Pi^{-1}\left[\phi_p^{l+1/2}-\Pi\left[\Phi_g^l\right]\right]. \tag{33}$$

This prolongation is distinctly different from typical "scaling" approaches [19] which are defined for the average scalar fluxes, $\bar{\phi}_p$ and $\bar{\Phi}_g$, as:

$$\bar{\Phi}_g^{p,l+1/2}=\bar{\Phi}_g^l\Pi^{-1}\left[\frac{\bar{\phi}_p^{l+1/2}}{\Pi\left[\bar{\Phi}_g^l\right]}\right] \tag{34}$$

The advantage of Eq. 33 is that it easily extends to any FEM basis function set while Eq. 34 does not have a natural extension to non-constant

shape functions. Within this work, CMFD is frequently used to denote the described NDA method using constant shape functions for the diffusion problem and the additive update of Eq. 33.

The particular form of the prolongation operator is derived with the goal to retain the fraction of the S_N solution that is outside of the span of the diffusion solution. To prove that Eq. 33 possesses this property, we write the scalar flux Φ_g^l as:

$$\Phi_g^l = \Phi_{g,\parallel}^l + \Phi_{g,\perp}^l, \tag{35}$$

where $\Phi_{g,\parallel}^l$ is within the span of the diffusion FEM basis and $\Phi_{g,\perp}^l$ is outside of it. Then, by definition of the projection and prolongation operators, it holds that:

$$\Phi_{g,\parallel}^l = \Pi^{-1}\left[\Pi\left[\Phi_g^l\right]\right] \Rightarrow \Phi_{g,\perp}^l = \Phi_g^l - \Pi^{-1}\left[\Pi\left[\Phi_g^l\right]\right]. \tag{36}$$

For the accelerated scalar flux $\Phi_g^{p,l+1/2}$ we want to retain $\Phi_{g,\perp}^l$ and accelerate the remainder with the prolonged diffusion flux, hence:

$$\Phi_g^{p,l+1/2} = \Pi^{-1}\left[\phi_p^{l+1/2}\right] + \Phi_{g,\perp}^l = \Phi_g^l + \Pi^{-1}\left[\phi_p^{l+1/2} - \Pi\left[\Phi_g^l\right]\right] \tag{37}$$

The algorithm for solving the nonlinear system of Eqs. 31 and 32 is described in Alg. 1. Initially, the angular flux is set to unity everywhere and the cross sections and closure terms are evaluated; subsequently a diffusion solve is performed; note that this leads to using a pure diffusion solution of the problem as initial guess for the first transport sweep. We opted to start with a diffusion solve to potentially reduce the total Picard iteration count by one by supplying a better initial guess to the S_N solution. Because of its low dimensionality, the cost of solving the diffusion system is relatively small. The diffusion problem is solved using MOOSE's preconditioned Jacobian-free Newton Krylov solver [1] that can solve both the fixed source and eigenvalue neutron diffusion problem. The preconditioning matrix does not contain cross-group scattering terms or fission terms by default, but options exist that allow assembling these block off-diagonal terms. Inversion of the preconditioning matrix usually utilizes the hypre algebraic multigrid (AMG) solver *boomeramg* [27]. Previous work [28] showed that solving of the NDA diffusion problem with AMG can be problematic because of the asymmetric drift closure term.

After the solution of the diffusion system, a single transport sweep is performed for obtaining a new estimate of the angular flux $\Psi_{g,m}^{l+1}$ on the

scattering source computed by using $\Phi_g^{p,l+1/2}$. A transport sweep denotes the inversion of the streaming and collision operator located on the left-hand-side of Eq. 1. The matrix collecting the contributions of the streaming and collision terms in Eq. 1 does not need to be assembled, because it is essentially lower triangular. Sweeping through all directions $\vec{\Omega}_m$ and mesh elements allows for an efficient way of obtaining $\Psi_{g,m}^{l+1}$ [16]. However, due to the large dimension of the S_N solution space, a single transport sweep is much more expensive than solving the diffusion equation iteratively. Therefore, the transport sweep is the essential unit of cost for obtaining the solution of the S_N equations. The Alg. 1 is known to converge rapidly within 7-15 Picard iterations for typical reactor physics problems. It should be noted that the influx from reflective boundary conditions in Eq. 32 is lagged by one iteration for the transport sweep potentially causing a reduction in the convergence rates in case the solution in the majority of the domain is strongly influenced by the reflective boundary conditions.

In the current Rattlesnake implementation, standard MOOSE residual evaluations are used to compute the source on which the sweep is performed. MOOSE's residual evaluations support second order meshes. Therefore, the correct answer of the S_N problem would be obtained after a sufficient number of sweeps even if the sweep is performed on a simplified mesh, e.g. by replacing curved faces with plane faces.

Algorithm 1. *Nonlinear diffusion acceleration algorithm.*

Set $l = 0$, $\Phi_g^l = 1$, $J_g^{out} = 0$, $\epsilon = 10tol$.
while $\epsilon > tol$ ***do***
    Project reaction rates, currents, and partial outflow currents.
    Evaluate diffusion cross sections, $\hat{D}_p^l$, α_p^l, *and* $\hat{\kappa}_p^l$.
    Solve low order eigenvalue problem using PJFNK solver capability.
    Prolongation for evaluating $Q_{s,g',g}$ *and* $Q_{f,g',g}$. *Transfer eigenvalue and compute* Q_g
    Obtain $\Psi_{g,m}^{l+1}$ *by performing a single transport sweep on* Q_g.
    Compute Φ_g^{l+1}.
    $\epsilon = \| \sum_{g=1}^{G} \nu\Sigma_{f,g} \left(\Phi_g^{l+1} - \Phi_g^l\right) \|_2$, $l = l + 1$.
end while

end

4. Fourier Analysis of the NDA Algorithm

In this section, a Fourier analysis of the linearized NDA algorithm described in Alg. 1 is performed for a single two-dimensional, quadrilateral mesh element with periodic boundary conditions. A total of three FEM basis function combinations is considered and denoted by (S_N-basis)/(diffusion basis): (bilinear)/(bilinear), (bilinear)/(constant), (constant)/(constant). The (bilinear)/(constant) is labeled as CMFD method because it uses a simple balance equation for accelerating the S_N system. For simplicity, coarse mesh acceleration is not considered, i.e. both the S_N equations and the diffusion equation are solved on the same quadrilaterial mesh cell. The linearization of the NDA algorithm is performed similarly to [20], but the mechanics of the implementation closely follow [16]. The Fourier analysis demonstrates that using identical FEM basis functions for discretizing the diffusion system can restore stability where the CMFD method is unstable. For the exemplified case of fine mesh acceleration, homogeneous material, and unity aspect ratio, the (bilinear)/(bilinear) NDA method is shown to be unconditionally stable.

4.1. Fourier Analysis of the NDA Algorithm: Theory

The Fourier analysis is performed for the one-group fixed source forms of Eqs. 5 and 24.The diffusion weak form is simplified to:

$$\begin{aligned}\left(\frac{1}{3\Sigma_t}\vec{\nabla}\phi^{l+1/2},\vec{\nabla}\phi^*\right)_{\mathcal{D}}+\left(\Sigma_a\phi^{l+1/2},\phi^*\right)_{\mathcal{D}}+\left(\kappa[\![\phi^{l+1/2}]\!],[\![\phi^*]\!]\right)_{\partial\mathcal{D}}\\ +\left(\left\{\frac{1}{3\Sigma_t}\vec{\nabla}\phi^{l+1/2}\cdot\vec{n}\right\},[\![\phi^*]\!]\right)_{\partial\mathcal{D}}+C_V[\Psi_m^l](\phi^*,\phi^{l+1/2})\\ +C_F[\Psi_m^l](\phi^*,\phi^{l+1/2})=0,\end{aligned}\tag{38}$$

where C_V and C_F are given by:

$$\begin{aligned}C_V[\Psi_m^l](\phi^*,\phi^{l+1/2}) &= \left(\hat{D}^l\phi,\vec{\nabla}\phi^*\right)_{\mathcal{D}}\\ C_F[\Psi_m^l](\phi^*,\phi^{l+1/2}) &= \left([\![\hat{\kappa}^l\phi^{l+1/2}]\!],[\![\phi^*]\!]\right)_{\partial\mathcal{D}}.\end{aligned}\tag{39}$$

The simplified S_N weak form reads:

$$\begin{aligned}\sum_{m=1}^{M}w_m\left(\Psi_m^{l+1},(-\vec{\Omega}_m\cdot\vec{\nabla}+\Sigma_t)\Psi_m^*\right)_{\mathcal{D}}\\ -\sum_{m=1}^{M}w_m\left\langle\Psi_m^{l+1,-},[[\Psi_m^*]]_m\right\rangle_{\partial\mathcal{D}}-\left(\Phi^{p,l+1/2},\frac{\Sigma_s}{4\pi}\Phi^*\right)_{\mathcal{D}}=0.\end{aligned}\tag{40}$$

At each iteration the angular flux and the scalar flux are separated as follows:

$$\begin{aligned} \Psi_m^{l+1} &= \Psi_m^{\infty} + \epsilon_m^{l+1} \\ \phi^{l+1/2} &= \phi^{\infty} + e^{l+1/2}, \end{aligned} \tag{41}$$

where the superscript ∞ indicates the exact iterative solution and ϵ_m^{l+1} and $e^{l+1/2}$ are the iterative errors at iterations $l+1$ and $l+1/2$, respectively. We note that the exact solution is flat in space and isotropic in angle and therefore it holds that:

$$\begin{aligned} \nabla\Psi_m^{\infty} = [[\Psi_m^{\infty}]] = [\![\phi^{\infty}]\!] = \vec{J}^{\infty} = 0 \\ \{\!\{\Psi_m^{\infty}\}\!\} = \Psi_m^{\infty},\ \{\!\{\phi^{\infty}\}\!\} = \phi^{\infty} \\ J^{\infty,out,\pm} = \Phi^{\infty}/4 \\ \phi^{\infty} = \Pi\left[\Phi^{\infty}\right]. \end{aligned} \tag{42}$$

Equations for the errors defined in Eq. 41 are obtained by first evaluating the weak forms Eqs. 38 and Eq. 40 with the exact iterative solution, Ψ_m^{∞} and ϕ^{∞}, and then subtracting the resulting weak forms from Eqs. 38 and Eq. 40:

$$\begin{aligned} &\left(\frac{1}{3\Sigma_t}\vec{\nabla}e^{l+1/2}, \vec{\nabla}\phi^*\right)_{\mathcal{D}} + \left(\Sigma_a e^{l+1/2}, \phi^*\right)_{\mathcal{D}} \\ &+ \left(\kappa[\![e^{l+1/2}]\!], [\![\phi^*]\!]\right)_{\partial\mathcal{D}} + \left(\left\{\frac{1}{3\Sigma_t}\vec{\nabla}e^{l+1/2}\cdot\vec{n}\right\}, [\![\phi^*]\!]\right)_{\partial\mathcal{D}} \\ &+\underline{C_V[\Psi_m^{\infty}+\epsilon_m^l](\phi^*, \phi^{\infty}+e^{l+1/2})} - C_V[\Psi_m^{\infty}](\phi^*,\phi^{\infty}) \\ &+\underline{C_F[\Psi_m^{\infty}+\epsilon_m^l](\phi^*, \phi^{\infty}+e^{l+1/2})} - C_F[\Psi_m^{\infty}](\phi^*,\phi^{\infty}) = 0, \end{aligned} \tag{43}$$

$$\begin{aligned} &\sum_{m=1}^{M} w_m\left(\epsilon_m^{l+1}, (-\vec{\Omega}_m\cdot\vec{\nabla}+\Sigma_t)\Psi_m^*\right)_{\mathcal{D}} \\ &-\sum_{m=1}^{M} w_m\left\langle \epsilon_m^{l+1,-}, [[\Psi_m^*]]_m\right\rangle_{\partial\mathcal{D}} - \left(E^{p,l+1/2}, \frac{\Sigma_s}{4\pi}\Phi^*\right)_{\mathcal{D}} = 0, \end{aligned} \tag{44}$$

where

$$\begin{aligned} E^{p,l+1/2} &= E^l + \Pi^{-1}\left[e^{l+1/2} - \Pi\left[E^l\right]\right] \\ E^l &= \sum_{m=1}^{M} w_m \epsilon_m^l. \end{aligned} \tag{45}$$

The underlined, nonlinear terms in Eq. 43 are now linearized with respect to the error terms about the exact iterative solution $(\Psi_m^\infty, \phi^\infty)$ by neglecting higher order terms in ϵ_m^{l+1} and $e^{l+1/2}$. The details of the linearization procedure can be found in Appendix A.

The final results after linearization of the volume C_V and face C_F closure terms are:

$$\begin{aligned} & C_V[\Psi_m^\infty + \epsilon_m^l](\phi^*, \phi^\infty + e^{l+1/2}) - C_V[\Psi_m^\infty](\phi^*, \phi^\infty) \\ & \approx -\left(\nabla\phi^*, \frac{1}{3\Sigma_t}\nabla\Pi\left[E^l\right] + \Pi\left[\vec{Y}^l\right]\right)_{\mathcal{D}}. \end{aligned} \tag{46}$$

$$\begin{aligned} & C_F[\Psi_m^\infty + \epsilon_m^l](\phi^*, \phi^\infty + e^{l+1/2}) - C_F[\Psi_m^\infty](\phi^*, \phi^\infty) \\ \text{SYW:} \quad & \approx \left(\left[\!\left[\phi^*\right]\!\right], \left[\!\left[(1/4-\kappa)e^{l+1/2} - 1/4\Pi\left[E^l\right]\right]\!\right]\right)_{\partial\mathcal{D}} \\ & + \left(\left[\!\left[\phi^*\right]\!\right], \left[\!\left[\Pi\left[Y^{l,out}\right] + \frac{\vec{n}_e\cdot\nabla\Pi\left[E^l\right]}{6\Sigma_t}\right]\!\right]\right)_{\partial\mathcal{D}} \\ \text{pNDA:} \quad & \approx \left(\left[\!\left[\phi^*\right]\!\right], \left[\!\left[\Pi\left[Y^{l,out}\right] - \kappa\Pi\left[E^l\right] + \frac{\vec{n}_e\cdot\nabla\Pi\left[E^l\right]}{6\Sigma_t}\right]\!\right]\right)_{\partial\mathcal{D}}, \end{aligned} \tag{47}$$

where the following quantities are defined for convenience:

$$\begin{aligned} (\vec{n}_e)^\pm &= \mp\vec{n} \\ \vec{Y}^l &= \sum_{m=1}^{M} w_m \vec{\Omega}_m \epsilon_m^l \\ Y^{l,out} &= \sum_{\vec{\Omega}_m\cdot\vec{n}>0} w_m \left|\vec{\Omega}_m\cdot\vec{n}\right| \epsilon_m^l. \end{aligned} \tag{48}$$

Using Eqs. 43, 44, 46, and 47, a linear FEM system for the errors can be constructed. Interestingly, when $\kappa = 1/4$, the linearized pNDA method algorithm becomes identical to SYW. For the remainder of this work, this method will be referred to as asymptotic diffusion (AD).

Until this point, the derivation of the linearized equations for the iterative error is very general, as it applies to any FEM bases combination applied to the diffusion and S_N equations. It is convenient to cast these equations in

operator notation to facilitate the Fourier analysis:

$$\begin{aligned} S_N: \quad & \mathbf{L}\epsilon_m^{l+1} = \mathbf{S}\left(E^l + \mathbf{\Pi}^{-1}\left(e^{l+1/2} - \mathbf{\Pi}E^l\right)\right) \\ \text{Diffusion:} \quad & \mathbf{A}e^{l+1/2} - \mathbf{V}_E\mathbf{\Pi}E^l - \mathbf{V}_Y\mathbf{\Pi}\vec{Y}^l - \mathbf{K}_e e^{l+1/2} \\ - \quad & \mathbf{K}_E\mathbf{\Pi}E^l - \mathbf{K}_E\mathbf{\Pi}Y^{l,out} = 0, \end{aligned} \tag{49}$$

where $\mathbf{L}$ collects the streaming, collision, and face term of the S_N equations, $\mathbf{S}$ collects the scattering contributions, $\mathbf{A}$ collects all contributions of the diffusion equations except the closure terms, $\mathbf{V}_E$ and $\mathbf{V}_Y$ collect the volume closure terms operating on E and Y, respectively, and $\mathbf{K}_e$, $\mathbf{K}_E$, and $\mathbf{K}_Y$ collect face closure terms operating on e, E, and Y^{out}, respectively.

For replacing E^l, $\vec{Y}^l$, and $Y^{out,l}$ with ϵ_m^l, the quadrature rules defined in Eqs. 45 and 48 are written in operator notation:

$$\begin{aligned} E^l &= \mathbf{D}_0\epsilon_m^l \\ \vec{Y}^l &= \mathbf{D}_1\epsilon_m^l \\ Y^{l,out} &= \mathbf{D}_1^{out}\epsilon_m^l. \end{aligned} \tag{50}$$

Using Eq. 50, Eq. 49 is recast as a system of equations in terms of ϵ_m and e:

$$\begin{aligned} S_N: \quad & \mathbf{L}\epsilon_m^{l+1} = \mathbf{S}\left(\mathbf{D}_0\epsilon_m^l + \mathbf{\Pi}^{-1}\left(e^{l+1/2} - \mathbf{\Pi}\mathbf{D}_0\epsilon_m^l\right)\right) \\ \text{Diffusion:} \quad & (\mathbf{A} - \mathbf{K}_e)e^{l+1/2} \\ = \quad & (\mathbf{V}_E\mathbf{\Pi}\mathbf{D}_0 - \mathbf{V}_Y\mathbf{\Pi}\mathbf{D}_1 + \mathbf{K}_E\mathbf{\Pi}\mathbf{D}_0 - \mathbf{K}_E\mathbf{\Pi}\mathbf{D}_1^{out})\epsilon_m^l. \end{aligned} \tag{51}$$

The Fourier analysis then proceeds as described in [16] by introducing phase matrices relating the iterative errors ϵ_m and e to their Fourier expansion coefficients $\tilde{\epsilon}_m$ and $\tilde{e}$:

$$\begin{aligned} \tilde{\epsilon}_m^l &= \mathbf{P}_\epsilon\epsilon_m^l \\ \tilde{e}^l &= \mathbf{P}_\mathbf{e}e^l. \end{aligned} \tag{52}$$

For the two considered function spaces, bilinear and constant, the phase matrices are given by:

Constant:

$$\mathbf{P} = \left[\ \exp(\tfrac{1}{2}i(\lambda_x\Delta x + \lambda_y\Delta y))\ \right]$$

Linear:

$$\mathbf{P} = \begin{bmatrix} 1 & 0 & 0 & 0 \\ 0 & \exp(i\lambda_x \Delta x) & 0 & 0 \\ 0 & 0 & \exp(i(\lambda_x \Delta x + \lambda_y \Delta y)) & 0 \\ 0 & 0 & 0 & \exp(i\lambda_y \Delta y) \end{bmatrix}, \tag{53}$$

where $i = \sqrt{-1}$, λ_x, λ_y are wave numbers in the x and y direction, and Δx and Δy are the dimensions of the mesh element.

Combining Eq. 51 and 52, an expression for the iteration step $\tilde{\epsilon}_m^l \rightarrow \tilde{\epsilon}_m^{l+1}$ can be derived as:

$$\begin{aligned} \tilde{\epsilon}_m^{l+1} &= \mathbf{Z}\tilde{\epsilon}_m^l \\ \mathbf{Z} &= \mathbf{L}^{-1}\mathbf{P}_\epsilon \mathbf{S}\left(\mathbf{D}_0\mathbf{P}_\epsilon + \mathbf{\Pi}^{-1}\left(\mathbf{X} - \mathbf{\Pi}\mathbf{D}_0\mathbf{P}_\epsilon\right)\right) \\ \mathbf{X} &= \left(\mathbf{A}\mathbf{P}_\mathbf{e} - \mathbf{K}_e\mathbf{P}_\mathbf{e}\right)^{-1} \\ &= (\mathbf{V}_E\mathbf{\Pi}\mathbf{D}_0 - \mathbf{V}_Y\mathbf{\Pi}\mathbf{D}_1 + \mathbf{K}_E\mathbf{\Pi}\mathbf{D}_0 - \mathbf{K}_E\mathbf{\Pi}\mathbf{D}_1^{out})\mathbf{P}_\epsilon. \end{aligned} \tag{54}$$

The spectral radius of the NDA method ρ can be inferred from the transition operator $\mathbf{Z}$ by:

$$\rho = \max_{\lambda_x,\lambda_y} |\mathrm{eig}(Z)| \text{ for } 0 < \lambda_x < \frac{2\pi}{\Delta x},\ 0 < \lambda_y < \frac{2\pi}{\Delta y}, \tag{55}$$

The spectral radius is evaluated by numerically searching for the maximum eigenvalue of $\mathbf{Z}$. For this purpose the numerical optimization capabilities of *MATHEMATICA* [29] are used. The implemented algorithm uses four different maximization algorithms, Nelder-Mead, Simulated Annealing, Differential Evolution, and Random Search; and picks the maximum of the results to decrease the likelihood of accepting a local maximum. In this work, the spectral radius is the central property of the NDA method as it indicates its effectiveness. A spectral radius smaller than unity is referred to as stable, while, somewhat arbitrary, a spectral radius smaller than 0.7 is referred to as effective.

4.2. Fourier Analysis of the NDA Algorithm: Results

Of particular interest is the change of the spectral radius with the scattering ratio:

$$\text{Scattering ratio: } c \equiv \frac{\Sigma_s}{\Sigma_t}, \tag{56}$$

and the optical cell thickness t:

$$\text{Optical cell thickness } t \equiv \Sigma_t \max(\Delta x, \Delta y). \tag{57}$$

A comparison of the pNDA-AD, pNDA-IP, and pNDA-MIP algorithms is conducted. Most importantly, the convergence properties of the NDA method depending on the pairing of the S_N and diffusion bases are investigated.

In Fig. 1, the spectral radius of the (bilinear)/(bilinear) FEM basis is plotted for varying scattering ratios and penalty modes versus the optical cell thickness. The (bilinear)/(bilinear) method leads to a unconditionally stable and effective acceleration method if the penalty coefficient is computed using the AD or MIP methods. In contrast, if the IP mode is selected, methods exhibit a second maximum in their ρ vs. t curves and become unstable for scattering ratios $c > 0.9$. The IP method exhibits instabilities because the penalty coefficient decreases monotonically with optical thickness. However, maintaining a sufficiently large penalty coefficient is essential in the interior penalty DGFEM discretization with weakly imposed continuity as too large inter-element jumps are permitted with small penalty coefficients.

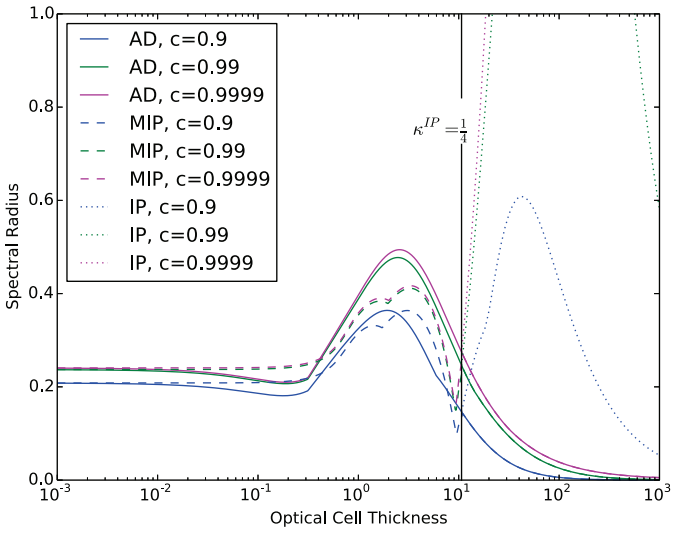

Figure 1: Spectral radius of the pNDA-AD, pNDA-IP and pNDA-MIP methods for (bilinear)/(bilinear) FEM basis obtained by Fourier analysis.

In Fig. 2 spectral radii for the pNDA-MIP with (constant)/(constant) shape functions are plotted. For intermediate optical thicknesses in the IP

region, i.e. $0.5 < t < 4/3$ the curves exhibit a steep increase. The peak magnitude of the spectral radius grows with the scattering radius with the expectation that for sufficiently large scattering ratios instabilities will be observed. The cause of this behavior is that in the region $0.1 < t < 4/3$ the penalty coefficient is too small to ensure proper convergence for the (constant)/(constant) shape function pairing. Further tests showed that in the limit of optically thin cells, smaller spectral radii can be obtained by having a smaller penalty coefficient. Therefore, we modified the penalty coefficient for the (constant)/(constant) case as follows:

$$\begin{aligned} \kappa_C^{IP} &= \kappa^{IP} f(t) \\ f(t) &= \begin{cases} 0.9 & t < 0.1; \\ 1.8 & t > 1.0; \\ 0.9(1 + \log_{10} \frac{t}{0.1}) & \text{else.} \end{cases} , \end{aligned} \tag{58}$$

where the factor of 0.9 was found to be near optimal in the thin cell limit. Results using penalty coefficients computed by Eq. 58 are presented in Fig. 3. These results are qualitatively similar to the (bilinear)/(bilinear) results with the exception of the spectral properties of the AD method for optically thin cells, where it becomes unstable. This behavior is unexpected since a loss of effectiveness and possibly stability is expected for optically thick cells. To understand this behavior better, Appendix B performs a fully analytical Fourier analysis in slab geometry focused on the thin cell limit. This Fourier analysis suggests that the thin cell limit of the spectral radius of the (constant)/(constant) pNDA-AD method is larger than unity for scattering ratios $c > 2/3$. As the (constant)/(constant) is not relevant for practical applications, these results have little consequence in practice, but are still valuable from an academic point of view. The (constant)/(constant) results underline the fact that a judicious choice of the penalty coefficient can influence the convergence properties significantly.

In Fig. 4 spectral radii for the (bilinear)/(constant) FEM basis are depicted. This combination of shape functions leads to a CMFD type acceleration method, where a constant diffusion method accelerates a high-order S_N discretization. Similar to the (constant)/(constant) case, the AD method shows instabilities for optically thin mesh cells. Even though the corresponding analysis is not performed for the CMFD scheme, it is reasonable to assume that the results of the Fourier analysis in Appendix B carry over to the CMFD scheme. The qualitative difference with respect to the (bilinear)/(bilinear) and (constant)/(constant) FEM pairings is that for optically

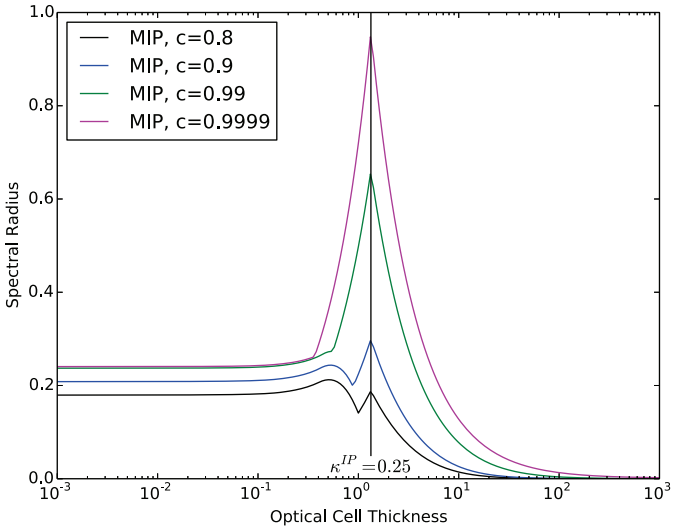

Figure 2: Spectral radius of the pNDA-AD, pNDA-IP and pNDA-MIP methods for (constant)/(constant) FEM basis obtained by Fourier analysis.

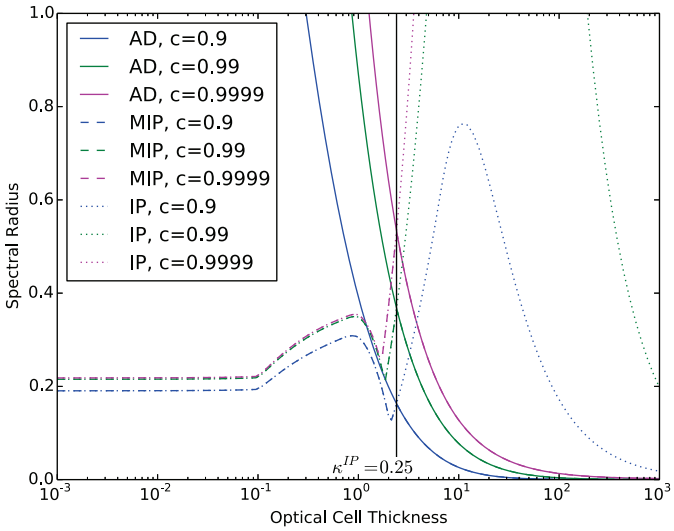

Figure 3: Spectral radius of the pNDA-AD, pNDA-IP and pNDA-MIP methods for (constant)/(constant) FEM basis obtained by Fourier analysis and κ^{IP} given by Eq. 58.

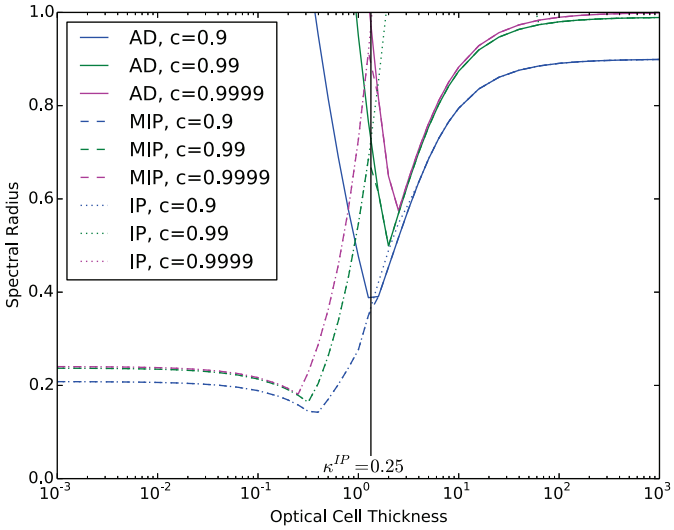

Figure 4: Spectral radius of the pNDA-AD, pNDA-IP and pNDA-MIP methods for (bilinear)/(constant) FEM basis obtained by Fourier analysis.

thick cells and scattering ratios close to one both MIP's and AD's spectral radii tend to unity. The CMFD method loses its effectiveness but it does not lose its stability. This is unexpected as instabilities of CMFD methods for optically thick cells are reported in the literature. Numerical experiments presented in section 5 will demonstrate that CMFD is indeed unstable and that Fourier analysis gives a qualitatively different prediction than numerical experiments. The reason for the discrepancy between the numerical experiments and the Fourier analysis is the linearization and (probably to a lesser extent) the assumption of periodicity of the solution.

The most important observation from the Fourier analysis is that the NDA method is unconditionally stable and effective if (bilinear)/(bilinear) and (constant)/(constant) FEM basis functions are used and the penalty coefficient is chosen to remain sufficiently large for optically thick cells. This corroborates the common wisdom that accerelation methods work better with closer similarity between the transport and diffusion discretizations. Effectiveness is lost if a CMFD type NDA scheme is applied, but Fourier analysis suggests that CMFD is still stable. Numerical results presented in section 5 show that in this regard Fourier analysis differs qualitatively from numerical experiments.

In addition, convergence properties of the presented NDA method are sensitive to the choice of the penalty coefficient as was shown in particular for the (constant)/(constant) FEM basis pairing. The methods' performance could be improved by adjusting κ^{IP}. However, in absence of a consistent theory of how to do this, the remainder of this work will employ the unmodified version of κ^{IP} given in Eq. 13.

It is worth noting that this Fourier analysis does not investigate two important properties of NDA methods: (1) performance if the diffusion mesh is coarser than the S_N mesh, (2) performance in the presence of strong material heterogeneities. The corresponding studies will be conducted using numerical experiments in the next section.

5. Numerical Experiments - Fixed Source Problems

Numerical experiments are conducted for the one-group, fixed source neutron transport equation discretized with a uniform quadrilaterial mesh. Due to the exponential growth of parameter combinations to investigate, this section focuses on the pNDA method and the modified interior penalty coefficient.

The number of mesh intervals along the x and y directions are chosen to be identical throughout the study. A two-dimensional test problem depicted in Fig. 5 is used for investigating the convergence properties of the presented NDA method. The problem is rectangular with an extent of $x = [0, X]$ and $y = [0, Y]$ in the x and y directions, respectively. Vacuum boundary conditions are applied on all boundary edges. The domain is uniformly subdivided into ten layers along the y-axis so that each layer has a thickness of $\Delta Y = Y/10$. The black region is referred to as region one, while the grey region is referred to as region two. Two parameters characterize the material properties in regions one and two: the scattering ratio c and the heterogeneity factor τ. Deviation of τ from unity makes the problem more challenging by introducing stronger material heterogeneity. The material properties in regions one and two are given by:

$$\begin{aligned} \Sigma_{t,1} &= \tau \\ \Sigma_{s,1} &= c\Sigma_{t,1} \\ \Sigma_{t,2} &= \frac{1}{\tau} \\ \Sigma_{s,2} &= c\Sigma_{t,2}. \end{aligned} \tag{59}$$

It is convenient to define the optical cell aspect ratio a that coincides with the domain optical aspect ratio:

$$a \equiv \frac{\Delta x}{\Delta y} = \frac{Y}{X}. \tag{60}$$

The mesh used for discretizing the S_N equations is nested within the diffusion mesh as depicted in Fig. 6. The coarsening factor pK relates the fine and coarse mesh spacing:

$$\begin{aligned} \Delta x_c &= K\Delta x \\ \Delta y_c &= K\Delta y. \end{aligned} \tag{61}$$

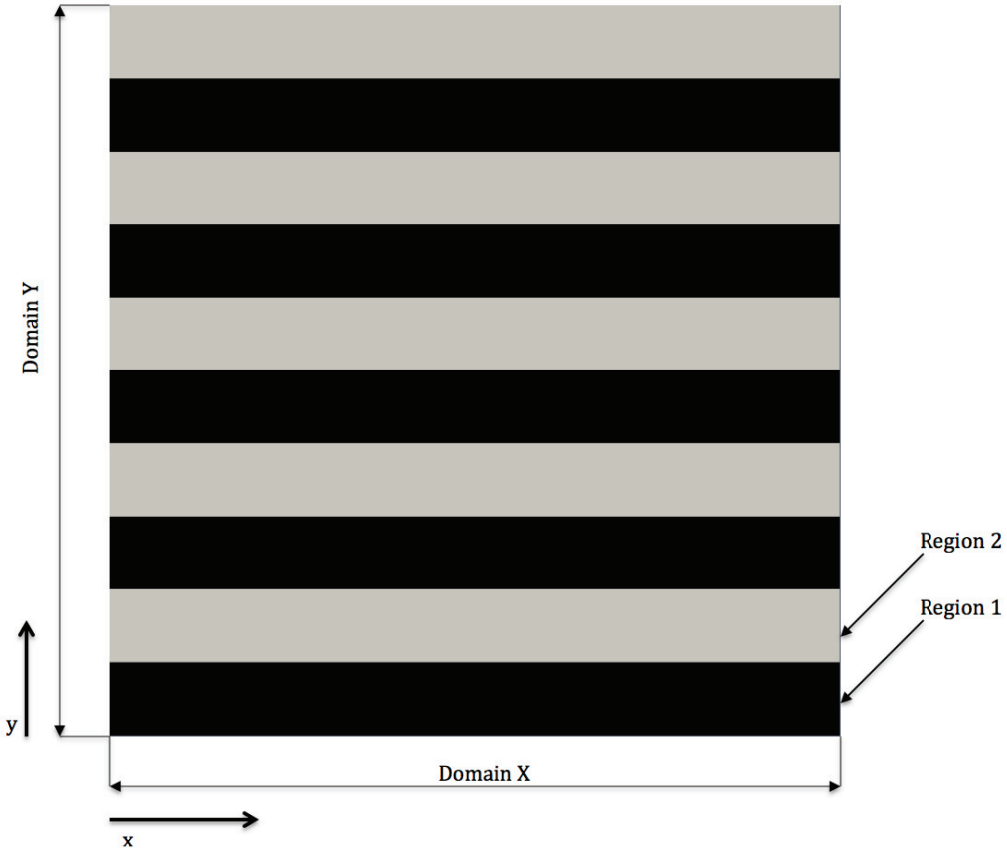

Figure 5: Geometry of the test problem used for numerical tests of the NDA method.

The solution of the transport problem is considered to be converged in iteration $L+1$ if $\delta_{L+1} = \|\Phi_g^{L+1} - \Phi_g^L\|_2 < 10^{-6}$. Subsequently, the numerical spectral radius ρ is estimated using the reduction of the L_2 difference over successive iterates:

$$\rho_l = \frac{\delta_{l+1}}{\delta_l}. \tag{62}$$

However, using only the last iterate $l = L$ is problematic if the convergence is not uniform, i.e. $\rho_l \neq \text{const}$. This is frequently encountered in cases with p2 and p4 meshes and high scattering ratios. Therefore, we resort to averaging

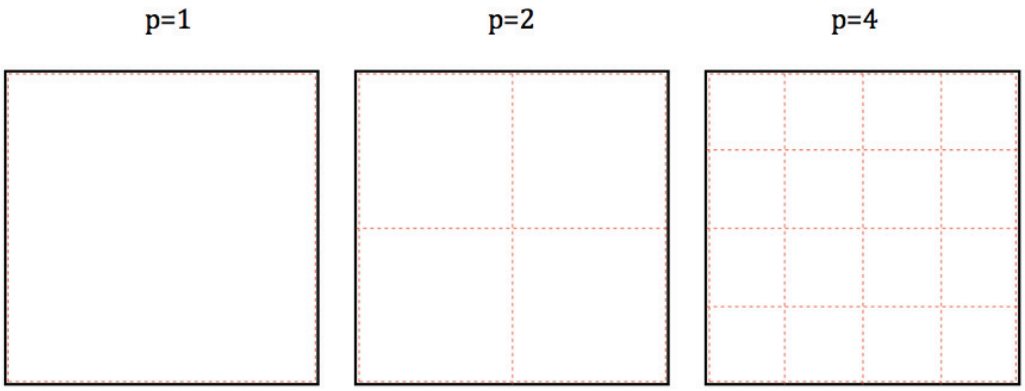

Figure 6: Mesh coarsening. The S_N mesh is indicated by dashed red lines and the diffusion mesh is indicated by solid black lines.

the spectral radius over several iterations:

$$\rho = \left(\prod_{n=1}^{N} \rho_{L-n} \right)^{1/N} \tag{63}$$

The range of the geometric mean is chosen as $N = \min(L/2, 6)$.

A maximum of 400 Picard iterations is permitted at which point the solve is aborted and considered failed. This implies that without looking at the convergence history it is impossible to distinguish slowly converging problems from truly non-converging problems. For ensuring proper convergence of the low order diffusion system, it is solved exactly using LU decomposition at each Picard iteration. The iterative error in the low order diffusion solve is made small enough to not affect the convergence of Picard iterations.

5.1. Regimes of Unconditional Stability of the NDA Method

This section demonstrates via numerical experiments that the presented NDA method is unconditionally stable, albeit not unconditionally effective, for the selected test problem regardless of τ and a if identical shape functions and meshes (p1) are used. For comparison, the lack of stability of the CMFD method is demonstrated to emphasize the advantages of using high order FEM bases for discretizing the diffusion equation.

In Fig. 7 the spectral radii of the (bilinear)/(bilinear) and (bilinear)/(constant) FEM pairings are plotted versus the optical cell thickness. Consistent with

the Fourier analysis presented in section 4, the (bilinear)/(bilinear) method is unconditionally stable and effective regardless of the scattering ratio. The spectral radius is always smaller than 0.5. In contrast, the (bilinear)/(constant) method loses effectiveness for all scattering ratios and stability for $c > 0.99$. For the highest scattering ratio $c = 0.9999$ effectiveness and stability are lost for $t > 2$ and $t > 5.5$, respectively.

While the (bilinear)/(bilinear) numerical results agree qualitatively with the FA, the FA analysis predicts that (bilinear)/(constant)'s spectral radius approaches $\rho = 1$ as $t \to \infty$. In fact, the (bilinear)/(constant) method becomes unstable as is illustrated in Fig. 8 plotting δ_l versus the Picard iteration number for a set of cases with t around 5. Curves with $t \geq 5.6875$ initially reduce δ_l, but then the iterative process becomes unstable with the onset of instability being visible as fluctuations in the curves. Slow convergence would be indicated by a straight, albeit slowly declining, line. It is important to stress here that differences between numerical results and the Fourier analysis are expected as it uses the **linearized** NDA method. Cases with smaller t, e.g. $t = 5.625$ also exhibit fluctuations but the convergence appears to be stable until the 10^{-6} convergence criterion is met.

Spectral radii for an aspect ratio of $a = 10$ are presented in Fig. 9. The important observation is that (bilinear)/(bilinear) retains the desirable property of unconditional effectiveness, while (bilinear)/(constant) remains only conditionally stable and effective.

As pointed out in Ref. [15], the spectral properties of acceleration methods tend to deteriorate in the presence of strong material heterogeneities. Within this work, the test case can be used for emulating the well-known periodical horizontal interface problem (PHI) by increasing the parameters τ and c keeping c close to unity [30]. The maximum number of iterations is increased to 2000 and the number of linear mesh subdivisions is fixed at 10 in order to evaluate the spectral properties in the vicinity of a spectral radius of unity. In Fig. 10 the spectral radii for various values of τ and c are depicted. Both FEM pairings lose effectiveness, albeit at different values of τ: for the highest scattering ratio (bilinear)/(bilinear) allows for $\tau \approx 5$, while (bilinear)/(constant) becomes ineffective for $\tau \approx 2$. Even though, the NDA method is not unconditionally effective in the presence of heterogeneities, using bilinear FEM for the diffusion system still holds an advantage over CMFD. The question of stability is answered by looking at the convergence history of representative (bilinear)/(bilinear) and (bilinear)/(constant) cases. In Fig. 11 the convergence history of the $\tau = 5$, $c = 0.9$ and $\tau = 1280$,

$c = 0.99999$ cases are presented. Both FEM pairings retain stability regardless of the choice of τ and c.

In summary, the (bilinear)/(bilinear) NDA method is unconditionally stable, but not unconditionally effective. Increasing the scattering ratio and the heterogeneity parameter τ simultaneously makes the spectral radius approach unity. The CMFD method is neither unconditionally stable, nor unconditionally effective. In particular, optically thick cells lead to both loss of effectiveness and stability.

5.2. Regimes of Conditional Stability of the NDA Method

The (bilinear)/(bilinear) NDA method loses unconditional stability if the diffusion mesh is coarser than the S_N mesh. In Figs. 12 and 13 spectral radii for problems with unity aspect ratio and coarsening factors two and four are depicted, respectively. Both the CMFD and NDA acceleration lose effectiveness and stability. However, using NDA still provides the advantage of extending the ranges of effectiveness and stability by roughly a factor of two and four, respectively, when compared to CMFD. Table 1 summarizes the optical thicknesses where stability and effectiveness is lost for both FEM pairings. Clearly, using linear FEMs in the diffusion system increases the range of applicability of NDA significantly. It needs to be stressed again that the diffusion system is of much smaller dimensionality such that increasing its execution cost is expected to have little impact on the execution time per Picard iteration.

For high scattering ratios, the ρ vs. t curves exhibit non-smoothness. This is attributed to non-uniform convergence ($\rho_l \neq$ const.) leading to the computed value of ρ to be dependent on the choice of which ρ_l to consider in Eq. 63. Representative examples of "rockier" convergence histories are plotted in Fig. 14.

5.3. Stability of Higher Order FEM Bases

In Fig. 15 the convergence properties of NDA using biquadratic FEM shape functions, i.e. the dyad of $\{1, x, x^2\}$ and $\{1, y, y^2\}$, are investigated. The resulting NDA algorithm is unconditionally stable and effective for unit aspect ratios and a homogeneous domain. In conjunction with the results obtained for the bilinear FEM shape functions, it appears that for structured quadrilateral grids and mild material heterogeneities using identical shape functions of at least first order yields an unconditionally stable and effective NDA method. However, this is not true in general.

In Fig. 16 the biquadratic shape functions are replaced by second order monomial shape functions: $\{1, x, y, xy, x^2, y^2\}$, in both the S_N and diffusion system. For smaller scattering ratios $c \leq 0.9$, NDA is stable and effective. For larger scattering ratios $c \geq 0.99$, NDA is stable and effective for very thick and thin cells, but exhibits instability for cells with an optical thickness between $t \approx 10..100$. For $c = 0.99$ only a single region of instability between $t = 20$ to 30 is observed. However, for $c = 0.9999$ an interesting change in behavior occurs. Within the range of $t = 10$ to 100 two regions of instability are observed, the first one is similar to the $c = 0.99$ case with optical cell thicknesses between $20 < t < 30$ and the second forms for optical thicknesses satisfying $50 < t < 106$. Right after stability is obtained for $t \approx 106$, the NDA algorithm enters a region of "fragmented" behavior, where perturbations in t as small as 10^{-4} change an effective convergence history exhibiting $\rho = 0.6$ to a non-convergent one. The behavior of the NDA algorithm is detailed in the inset plot in Fig. 16. This fragmented region extends from $t = 106$ to $t = 107$.

By numerical experiment it is found that this behavior can be attributed to the NDA algorithm converging to the solution only from certain initial guesses. Two cases with optical thicknesses of $t1 = 106.1125$ (case one) and $t2 = 106.1125625$ (case two) are used to demonstrate this behavior and the convergence histories are plotted in Fig. 17. The first case converges using the presented NDA algorithm without modification even though initial oscillations[2] are observed; note that this NDA algorithm uses the pure diffusion solution of the problem as initial guess for the first transport sweep. However, if we use a random initial setting for the closure terms in the initial diffusion solve, and provide the result of this as initial guess for the first transport update, case 1 does not converge. This case is labeled as random initial guess in Fig. 17, even though in reality the angular flux is initialized randomly and then used to compute the closure terms and cross sections before the first diffusion solve.

For the second case using the diffusion solution as initial guess does not lead to convergence and instead oscillations are observed. Note that the apparent increase in frequency is caused by the logarithmic scaling of the x-axis. However, if instead of the pure diffusion solution a loosely converged

[2]The term oscillations is used due to the absence of a better description. The authors do not necessarily imply that the curves are periodic.

S_2 transport solution is used as initial guess, convergence is achieved for the second case.

The combined results depicted in Fig. 17 demonstrate that the NDA algorithm converges to the right answer only from certain initial guesses. In addition, we demonstrate in Fig. 17 that convergence for case 2 can be restored if instead of a single transport sweep per Picard iteration two transport updates are used.

Both approaches, the S_2 initial guess and allowing two transport updates per Picard iteration, present effective remedies for achieving convergence in cases where the original NDA algorithm fails to converge.

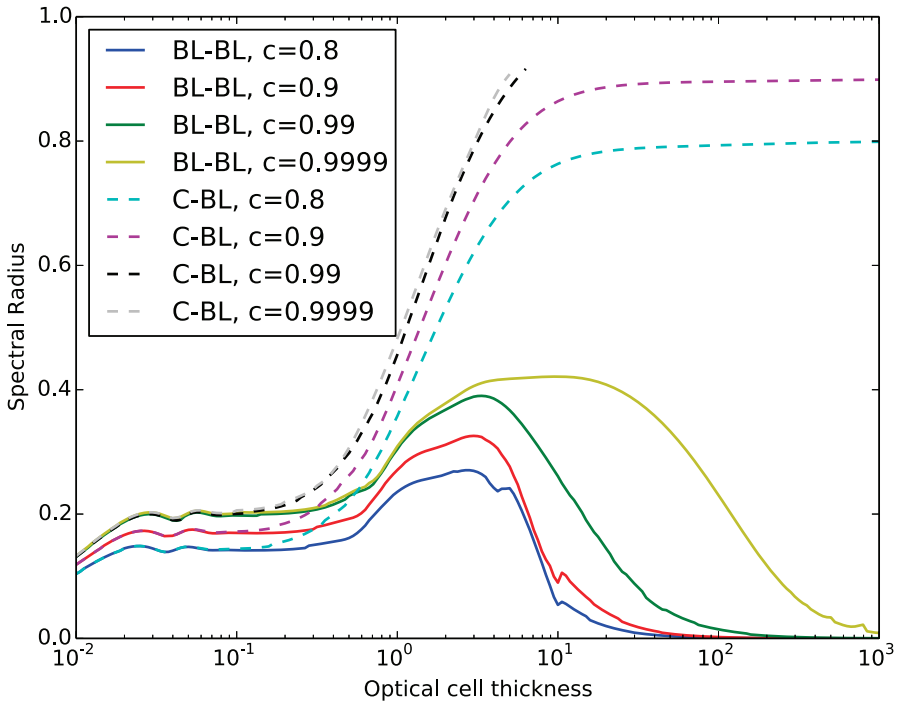

Figure 7: Spectral radius of (bilinear)/(bilinear) and (bilinear)/(constant) FEM pairings for homogeneous test case ($\tau = 1$) with $a = 1$ and p1.

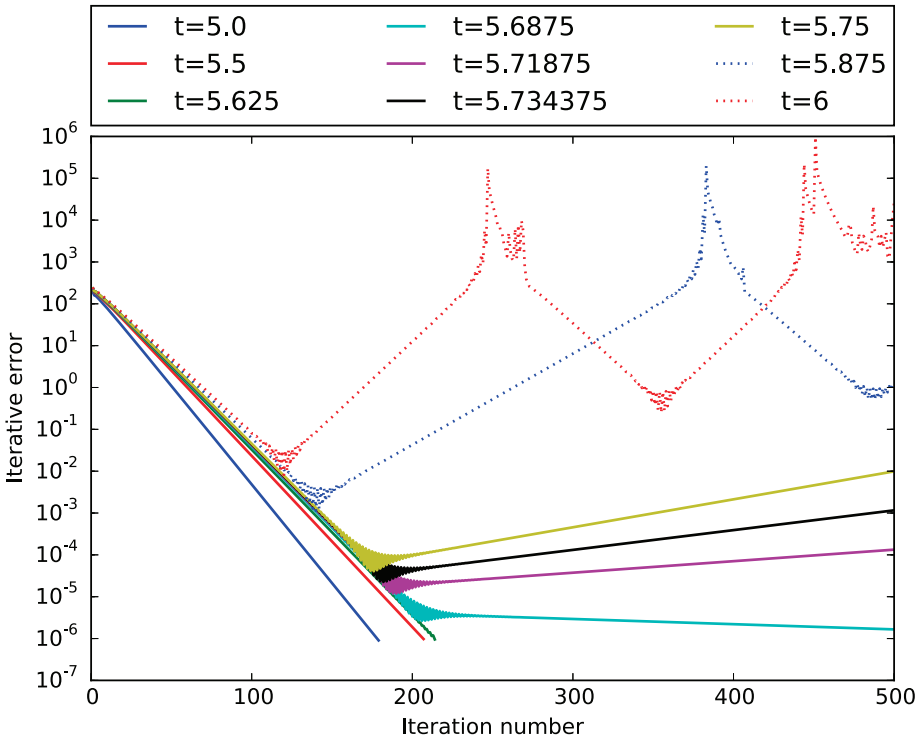

Figure 8: Convergence history of the (bilinear)/(constant) FEM pairing with $a = 1$, $c = 0.9999$ and p1.

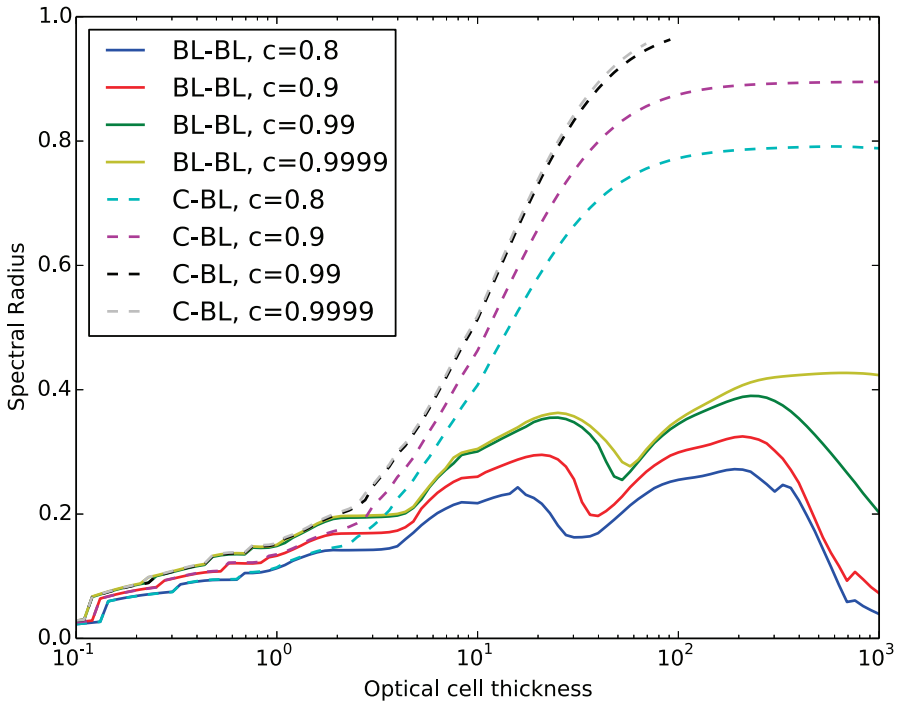

Figure 9: Spectral radius of (bilinear)/(bilinear) and (bilinear)/(constant) FEM pairings for homogeneous test case ($\tau = 1$) with $a = 10$ and p1.

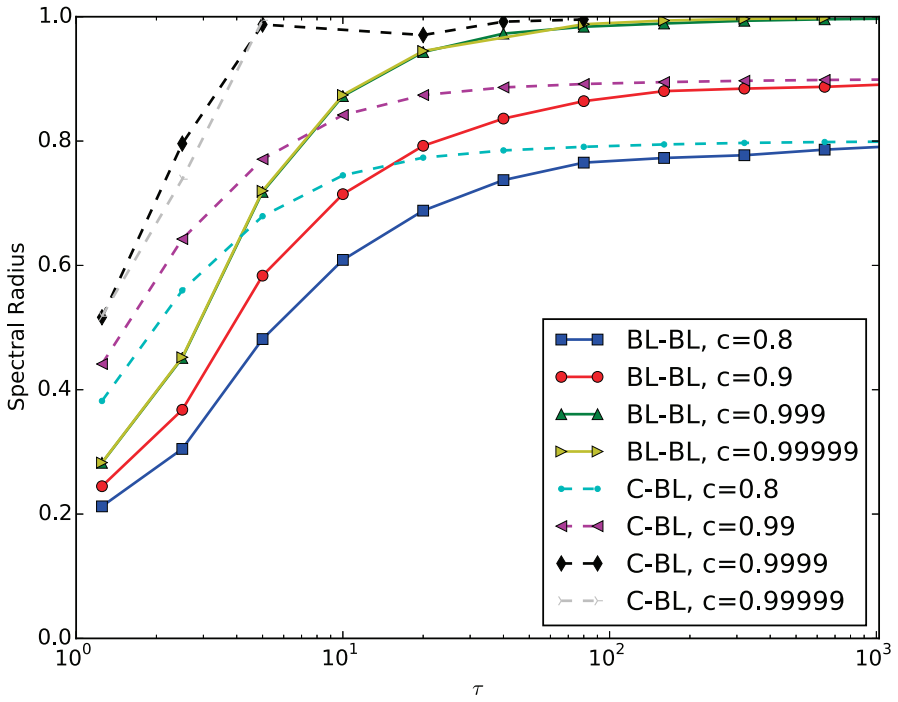

Figure 10: Spectral radius of (bilinear)/(bilinear) and (bilinear)/(constant) FEM pairings for PHI test case for varying scattering ratios ($a = 1$ and p1) plotted against τ.

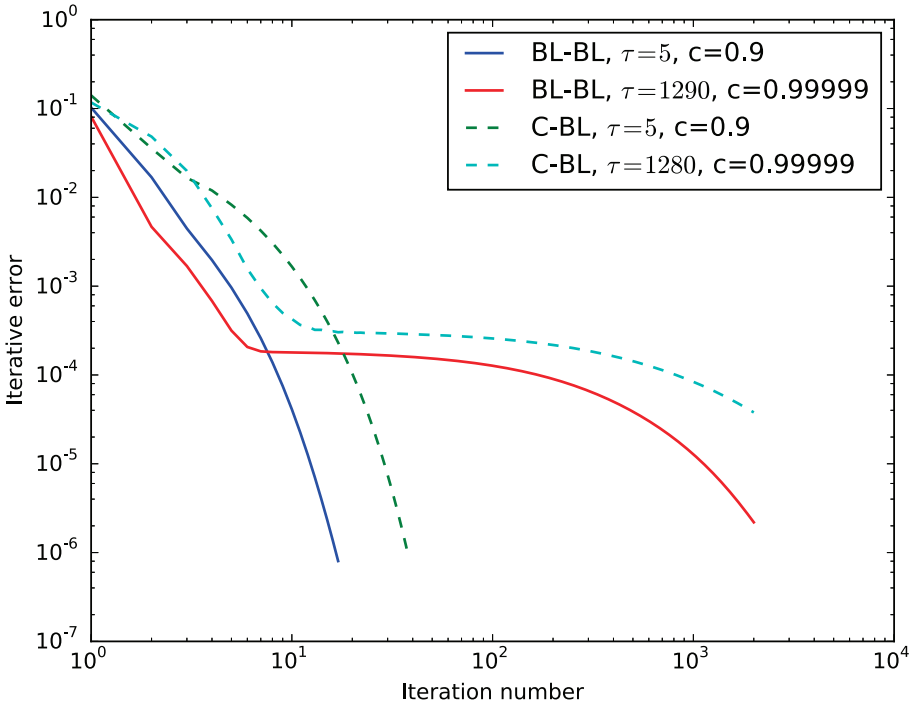

Figure 11: Convergence history for (bilinear)/(bilinear) and (bilinear)/(constant) FEM pairings for PHI test case.

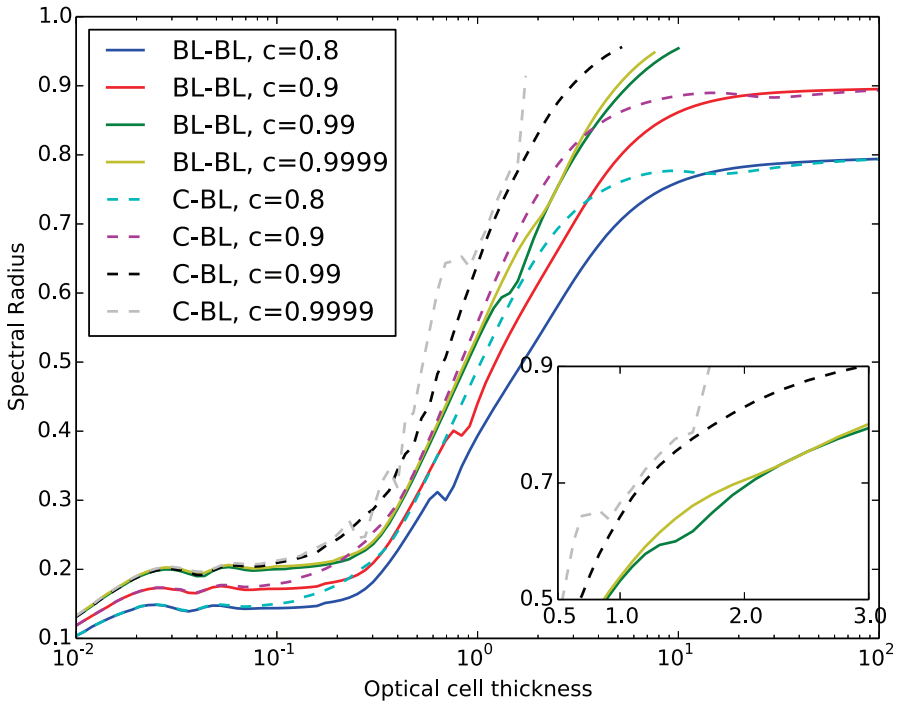

Figure 12: Spectral radius of (bilinear)/(bilinear) and (bilinear)/(constant) FEM pairings for homogeneous test case ($\tau = 1$) with $a = 1$ and p2.

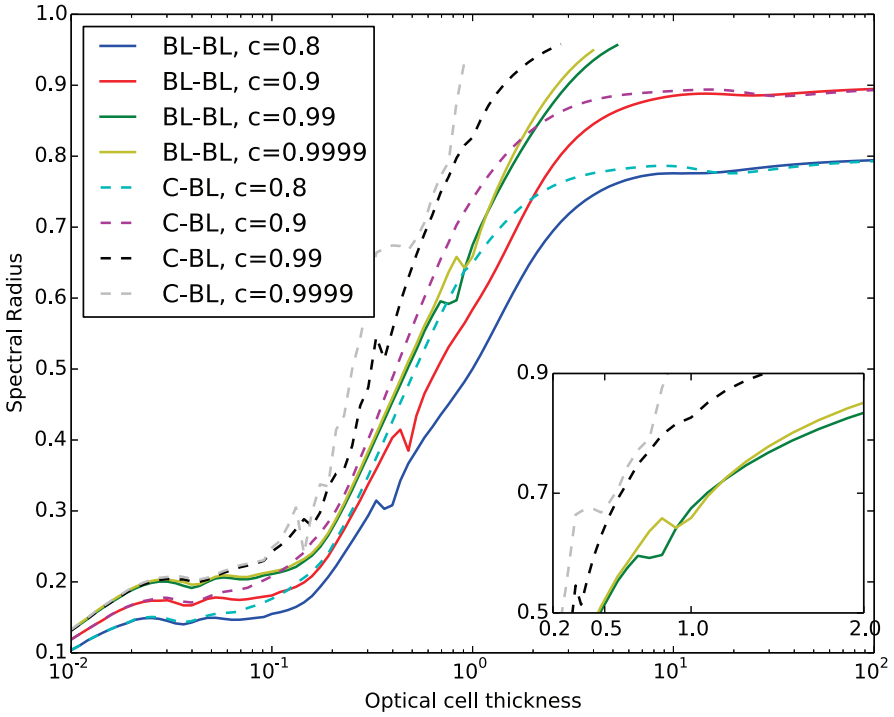

Figure 13: Spectral radius of (bilinear)/(bilinear) and (bilinear)/(constant) FEM pairings for homogeneous test case ($\tau = 1$) with $a = 1$ and p4.

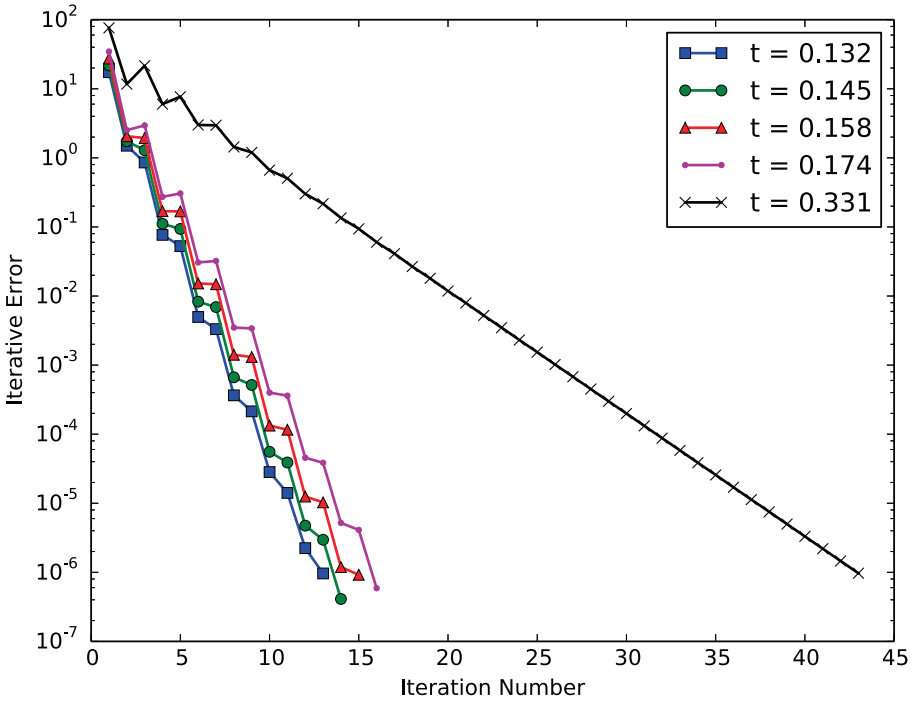

Figure 14: Convergence histories for (bilinear)/(constant) FEM pairing, p4, and $c = 0.9999$ for various optical cell thicknesses t.

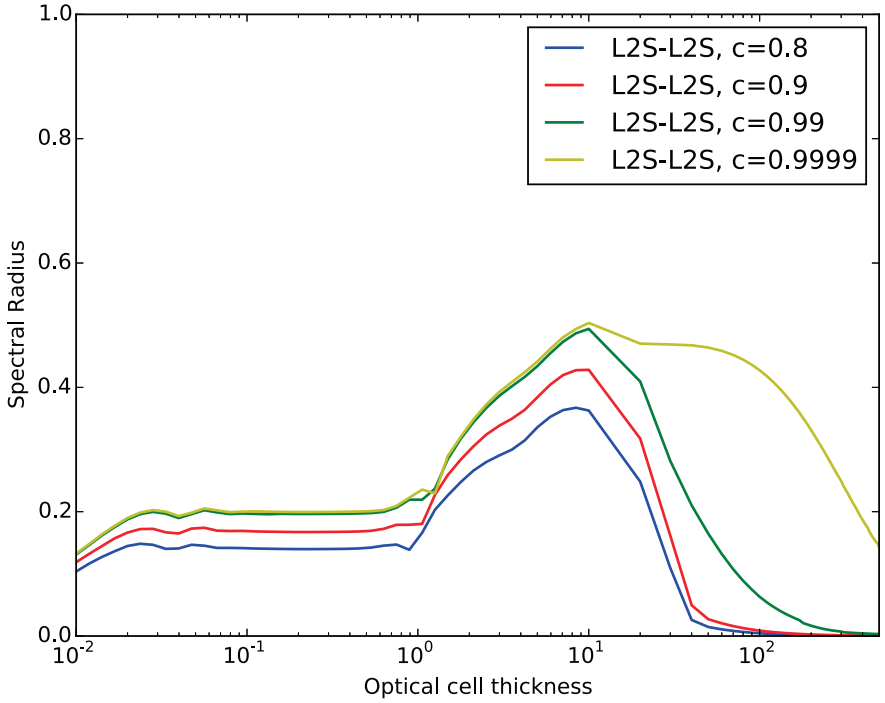

Figure 15: Spectral radius of the (biquadratic)/(biquadratic) FEM pairing for the for homogeneous test case ($\tau = 1$) with $a = 1$ and p1.

		Stability	Effectiveness $\rho < 0.7$
p1	(bilinear)/(bilinear)	n.a.	n.a.
	(bilinear)/(constant)	5-6	2.1
p2	(bilinear)/(bilinear)	8-9	2.0
	(bilinear)/(constant)	≈ 2	1.1
p4	(bilinear)/(bilinear)	4-4.5	1.1
	(bilinear)/(constant)	≈ 1	0.58

Table 1: Spectral radius beyond which effectivenss and stability are lost for (bilinear)/(bilinear) and (bilinear)/(constant) FEM pairings for homogeneous test case ($\tau = 1$), $a = 1$ and $c = 0.9999$. Stability limits are approximate because the finite number of NDA iterations lead to a maximum observable spectral radius.

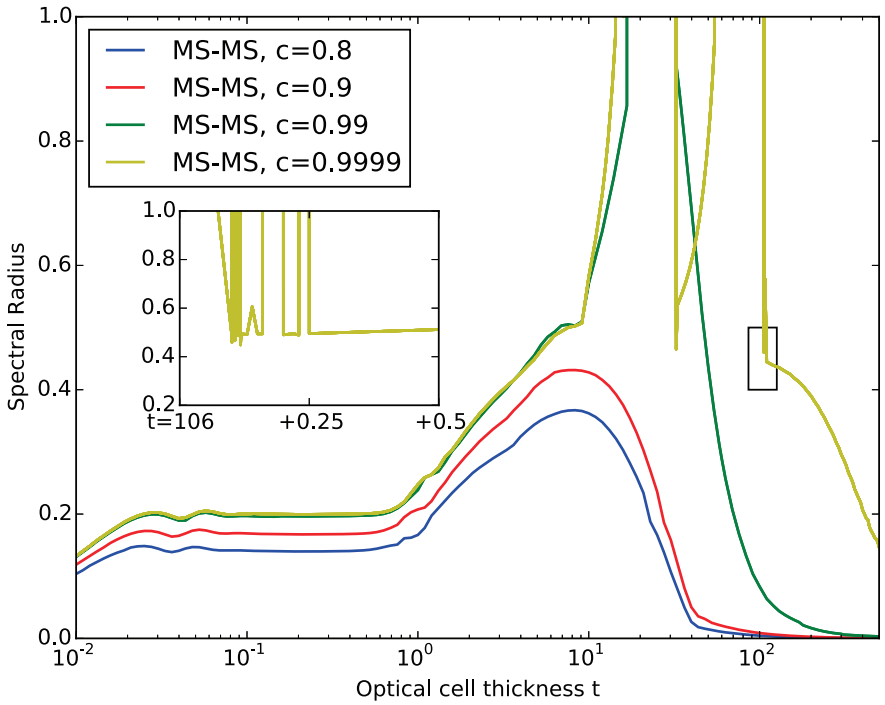

Figure 16: Spectral radius of the (second monomial)/(second monomial) FEM pairing for the for homogeneous test case ($\tau = 1$) with $a = 1$ and p1.

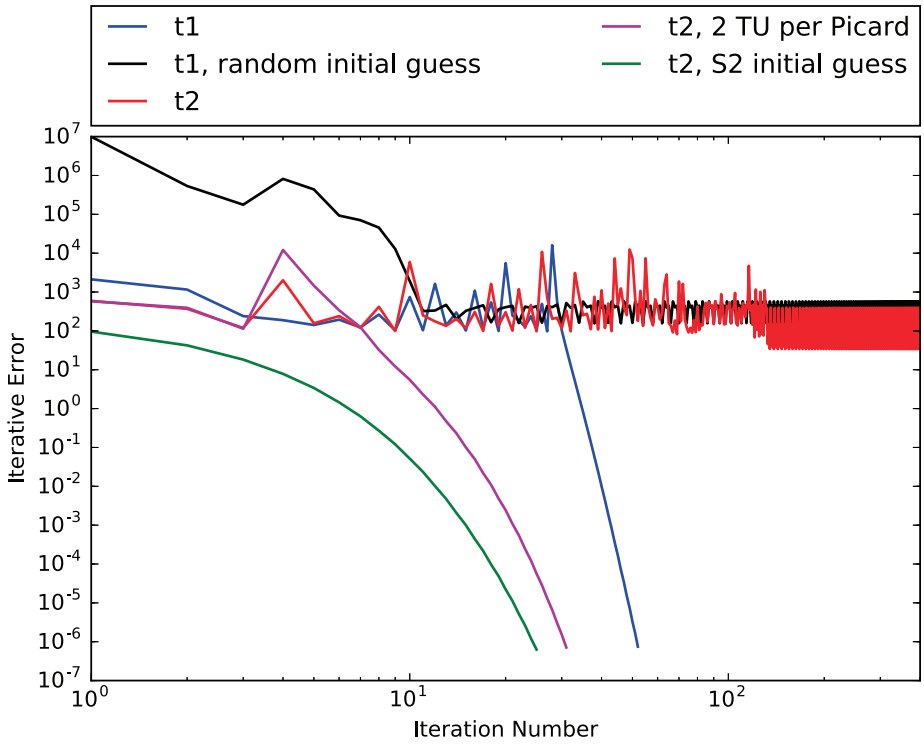

Figure 17: Convergence histories for the case described in Fig. 16 for two optical cell thicknesses $t1 = 106.1125$ and $t2 = 106.1125625$. The difference of the two optical cell thicknesses is $\Delta t = 6.25 \times 10^{-5}$. While $t1$ converges without modification of the algorithm $t2$ does not. However, when using 2 transport updates (TU) per Picard iteration or when a loosely converged S_2 solution is used as initial guess, convergence is achieved.

6. Numerical Experiments - Eigenvalue Problem

In this section, numerical results are presented for the C5G7 benchmark problem [31]. As in section 5, the S_8 level symmetric quadrature is utilized. For discretizing the S_N problem an unstructured triangular mesh depicted for a single MOX assembly in Fig. 18 is used featuring roughly $120,000$ elements. In contrast, the diffusion equation is discretized either on the same mesh or on a rectangular mesh coincident with the pin cell boundaries (2,601 elements). The triangular mesh is nested within the rectangular pin-cell mesh. Further, seven energy groups are used for the S_N problem, while the diffusion system employs either the same energy group structure or a two group structure collapsing the first three groups (fast groups) into coarse group one and the last four groups (thermal groups with upscattering) into coarse group two. It is important to split the groups such that no upscattering occurs across the coarse energy group boundary. Initial tests use an incorrect splitting of four groups and three groups leading to slower convergence overall and even stalling convergence. At each Picard iteration, the diffusion eigenvalue problem is solved using MOOSE's PJFNK solver. For circumventing problems with selecting correct preconditioner settings for the linear GMRES iterations, an exact LU inversion is performed such that linear iterations converge after one iteration. Sweeping through all group is performed using a Jacobi-type iteration scheme, i.e. the downscattering source is updated only after all groups are solved. This allows easy parallelization of the algorithm. The nonlinear relative and absolute iterative tolerances are set to 10^{-6} and 10^{-9}, respectively. It needs to be stressed that all presented results are obtained for a single processor and therefore solver asynchronicity is not an issue in the presented work. The S_N system uses linear shape functions, while the diffusion system uses either constant shape functions (CMFD)[3], or linear shape functions (NDA). Convergence of the fission source is measured as the absolute L_2 difference between subsequent Picard iterates. The fission source error is plotted versus the iteration number in Fig. 19. Table 2 summarizes the total number of Picard iterations required for convergence depending on the solver settings.

CMFD and NDA appear to be stable for all combinations of diffusion meshes and energy group structures. In general, reducing the complexity of

[3]To reiterate, the CMFD method uses an additive update and is therefore not identical to the traditional CMFD method.

the diffusion system reduces the effectiveness of the NDA method. When using a fine mesh and seven energy groups for the diffusion system, the NDA and CMFD methods are stable and effective (8 iterations for convergence to 10^{-6} fission source difference) and virtually no advantage is gained when the diffusion system is discretized using linear shape functions. However, when coarsening the diffusion mesh, NDA exhibits only a moderate increase in number of Picard iterations, while CMFD's iteration count doubles. This result is of great importance because coarse diffusion acceleration is the target application of the presented NDA method. Coarsening the group structure affects both methods' effectiveness equally as the iteration count more than doubles revealing that reducing the complexity in energy has a larger effect on the Picard iteration count. Finally, using a coarse mesh in conjunction with two energy groups increases the iteration count only marginally when compared to the coarse energy group structure only case. Again, NDA requires fewer iterations than CMFD but the difference is not as pronounced as when seven groups are used for the diffusion system.

The immediate conclusion from the numerical experiment is that NDA with a fine group and coarse mesh diffusion system should be the algorithm of choice, because the Picard iteration count increases only slightly while the cost for solving the low order diffusion problem reduces significantly: 25% increase in Picard iteration count but a reduction of elements in the diffusion system by roughly a factor of 50. Considering the S_8 angular quadrature the diffusion system has 2,000 times fewer DOFs as the transport system[4]. Under these circumstances, the low order problem could be solved using Chebychev or Wielandt shift accelerated power iterations where the within group equations are inverted using a direct solver. Handling even a large number of groups should then be possible.

The two-dimensional C5G7 problem is primarily chosen to demonstrate the ability of solving the diffusion problem on a coarser mesh and with a coarser group structure while retaining stability. It is noted that the dominance ratio of the eigenvalue problem is irrelevant to the convergence properties of NDA.

[4]This ratio would be doubled because of the loss of angular symmetry from 2D to 3D geometries.

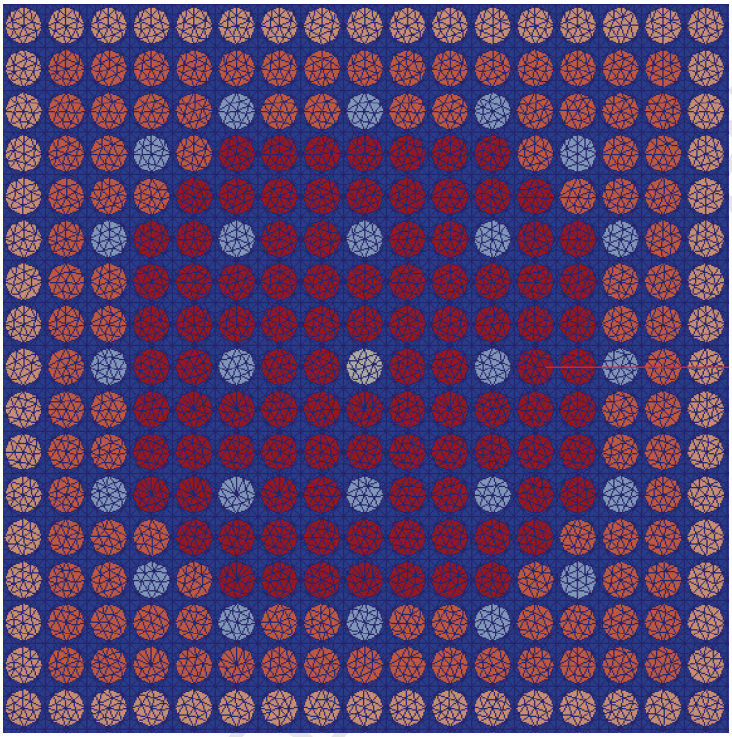

Figure 18: Triangular mesh for a single C5G7 MOX assembly.

	CMFD		NDA	
	Fine mesh	Coarse Mesh	Fine Mesh	Coarse Mesh
Fine group	8	16	8	10
Coarse group	18	21	18	19

Table 2: Picard iterations required for convergence.

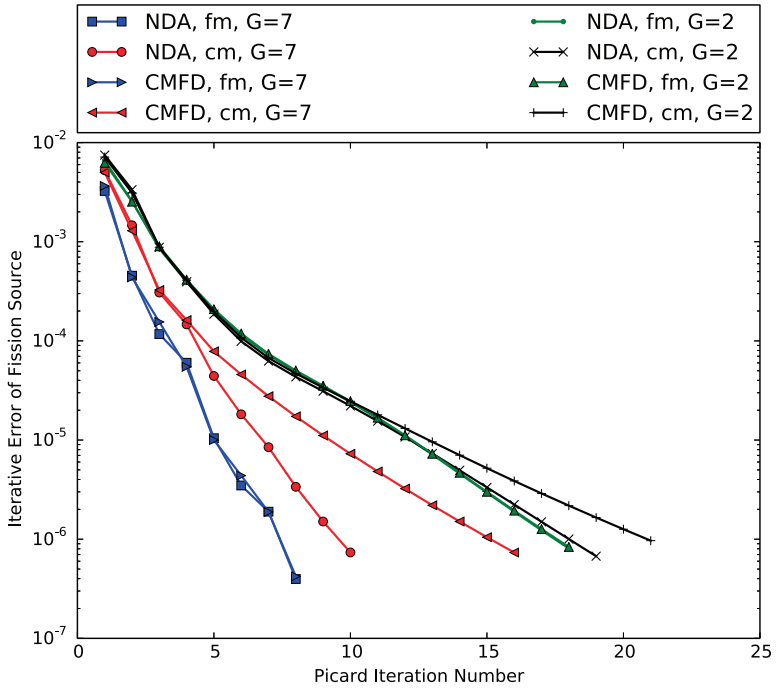

Figure 19: Fission source error plotted versus iteration number for C5G7-2D. The diffusion system's discretization is varied using fine/coarse meshes (fm, cm) and fine/coarse energy group structures (G=7, G=2) and various combinations thereof.

7. Conclusions

This work presents a flexible nonlinear diffusion acceleration method that discretizes both the S_N and diffusion equations using the discontinuous finite element method. In contrast to CMFD methods that use only a balance equation for acceleration of the S_N equations, the presented NDA method discretizes a full diffusion equation using an arbitrary FEM basis. Customary for NDA method, the diffusion problem can be solved on a coarser mesh than the transport problem with the only restriction that the coarser mesh must be nested within the finer mesh. A general FEM framework is laid out that allows the definition of consistent projection and prolongation operators. The projection operator is then utilized to define the general notion of *consistency* of the S_N and diffusion scalar fluxes. In contrast to standard CMFD schemes, the prolongation operator uses an additive update ensuring that only the subset of the S_N FEM space is altered that is within the span of the diffusion FEM space.

A Fourier analysis for a single quadrilateral cell with periodic boundary conditions and (bilinear)/(bilinear) and (bilinear)/(constant) FEM bases for the S_N and diffusion problem, respectively, is performed. For this purpose the NDA iterations are linearized about the iterative solution. The main conclusions from the Fourier analysis is that the (bilinear)/(bilinear) and (constant)/(constant) FEM pairing are unconditionally stable and effective, i.e. stable for all optical cell thicknesses, while the (bilinear)/(constant) method becomes ineffective for optical thicknesses between five and ten, but retains stability. This research indicates that the (bilinear)/(constant) methods become in fact unstable, but the Fourier analysis does not capture this behavior most likely due to the linearization around the exact iterative solution. The Fourier analysis confirms the common wisdom originally stated for DSA methods that acceleration methods perform better as the similarity between the S_N and diffusion discretizations increases.

Numerical experiments based on the one-group, fixed source problem are performed for homogeneous and strongly heterogeneous problems (periodic horizontal interface problem). Most of the presented results focus on the comparison of the (bilinear)/(bilinear) and the (bilinear)/(constant) FEM pairing. The main conclusion is that the (bilinear)/(bilinear) method is unconditionally stable and effective if identical meshes are used for the S_N and diffusion problems and the problem is only mildly heterogeneous. If the probem's heterogeneity becomes too strong, effectivenss is in general lost, but

stability is retained. The (bilinear)/(constant) pairing loses both effectiveness and stability for optically thick cells even if the S_N and diffusion mesh are identical. In case of coarse mesh acceleration, the (bilinear)/(bilinear) method loses stability and effectiveness, but both the regions of stability and effectiveness are extended by a factor of two when compared to the (bilinear)/(constant) FEM pairing.

Higher order results are obtained using biquadratic and second order monomial shape functions for the discretization of the S_N and diffusion system. For biquadratic shape functions, it is found that the NDA algorithm is stable and effective regardless of the optical cell thickness. However, for second order monomial shape functions, only problems with scattering ratios $c \leq 0.9$ are unconditionally stable and effective, while for a scattering ratio of $c = 0.99$ an interval between $t = 20 - 30$ mfp cell thickness exhibits instabilities. For the highest tested scattering ratio $c = 0.9999$ the convergence properties exhibit a curious behavior. For $t < 100$ two regions of instability are observed, $t = 20 - 30$ and $t = 50 - 106$, and for $106 < t < 107$ convergence to the solution strongly depends on the initial guess. Finally, regardless of the scattering ratio the spectral radius approaches zero in the thick cell limit.

Finally, the NDA method is used for solving the C5G7 multigroup, eigenvalue problem, a representative LWR geometry, using fine and coarse meshes and energy group structures for the discretization of the diffusion system. The results indicate that the presented method is stable for all combinations of diffusion shape functions, meshes, and energy group structures. In addition, no underrelaxation of the Picard iteration strategy is required for convergence. A reduction of effectiveness ranging from moderate (+25% Picard iteration count) to significant (+165% Picard iteration count) is observed when the diffusion system's fidelity is reduced. Using identical FEM bases for the S_N and diffusion equation, the increase in iteration count is moderate when coarsening the diffusion mesh, but for CMFD the iteration count doubles.

8. Acknowledgements

This manuscript has been authored by Battelle Energy Alliance, LLC under Contract No. DE-AC07-05ID14517 with the U.S. Department of Energy. The United States Government retains and the publisher, by accepting the article for publication, acknowledges that the United States Government retains a nonexclusive, paid-up, irrevocable, world-wide license to publish or reproduce the published form of this manuscript, or allow others to do so, for United States Government purposes.

Appendix A. Linearization of Closure Relationships for Fourier Analysis

For the linearization of the closure relationships, it is most convenient to assume that the angular space is continuous, and quadrature rules are replaced by the corresponding integrals, e.g. $\sum_{m=1}^{M} w_m \rightarrow \int_{4\pi} d\vec{\Omega}_m$. A recurring theme within this section is linearization of fractions:

$$\frac{x}{y}z = \frac{x^\infty + \delta x}{y^\infty + \delta y}(z^\infty + \delta z) \approx \frac{x^\infty}{y^\infty}z^\infty + \frac{x^\infty}{y^\infty}\delta z + \frac{z^\infty}{y^\infty}\delta x - \frac{x^\infty y^\infty}{(y^\infty)^2}\delta y. \tag{A.1}$$

Appendix A.1. Linearization of the Volume Closure

The volume closure term $C_V\left[\Psi_m^\infty + \epsilon_m^l\right](\phi^*, \phi^\infty + e^{l+1/2})$ is given by:

$$\begin{aligned} & C_V\left[\Psi_m^\infty + \epsilon_m^l\right](\phi^*, \phi^\infty + e^{l+1/2}) \\ = & \left(\nabla\phi^*, -\frac{\int_{4\pi}\frac{1}{3\Sigma_t}\nabla\Pi\left[\Psi_m^\infty + \epsilon_m^l\right] + \hat{\Omega}\Pi\left[\Psi_m^\infty + \epsilon_m^l\right]d\hat{\Omega}}{\Pi\left[\Phi^\infty + E^l\right]}\left(\phi^\infty + e^{l+1/2}\right)\right). \end{aligned} \tag{A.2}$$

Applying the definition of scalar flux and currents, and regrouping Eq. A.2 leads to:

$$\begin{aligned} & C_V\left[\Psi_m^\infty + \epsilon_m^l\right](\phi^*, \phi^\infty + e^{l+1/2}) \\ = & \left(\nabla\phi^*, -\frac{\frac{1}{3\Sigma_t}\nabla\Pi\left[\Phi^\infty\right] + \Pi\left[\vec{J}^\infty\right] + \frac{1}{3\sigma_t}\nabla\Pi\left[E^l\right] + \Pi\left[\vec{Y}^l\right]}{\Pi\left[\Phi^\infty\right] + \Pi\left[E^l\right]}\left(\phi + e^{l+1/2}\right)\right). \end{aligned} \tag{A.3}$$

In Eq. A.3 we note that $\frac{1}{3\Sigma_t}\nabla\Pi\left[\Phi^\infty\right] + \Pi\left[\vec{J}^\infty\right] = 0$ because the exact solution is constant in space and isotropic in angle. Using Eq. A.1 and the definition of consistent S_N and diffusion scalar fluxes, Eq. 15, we obtain:

$$\begin{aligned} & C_V\left[\Psi_m^\infty + \epsilon_m^l\right](\phi^*, \phi^\infty + e^{l+1/2}) \\ \approx & -\left(\nabla\phi^*, \frac{1}{3\Sigma_t}\nabla\Pi\left[E\right]^l + \Pi\left[\vec{Y}^l\right]\right). \end{aligned} \tag{A.4}$$

Appendix A.2. Linearization of the SYW Face Closure

The SYW closure is given by:

$$\begin{aligned} C_{F,SYW}\left[\Psi_m^l\right](\phi^*,\phi^{l+1/2}) &= \left([\![\phi^*]\!],[\![\hat{\kappa}_{SYW}(\Psi_m^l)\phi^{l+1/2}]\!]\right), \\ \hat{\kappa}_{SYW}(\Psi_m^l) &= \frac{\int\limits_{\vec{n}_e\cdot\hat{\Omega}>0} d\hat{\Omega}\left|\vec{n}_e\cdot\hat{\Omega}\right|\Pi\left[\Psi_m^l\right]}{\int_{4\pi} d\hat{\Omega}\Pi\left[\Psi_m^l\right]} \\ &+ \frac{1}{2}\frac{\frac{1}{3\Sigma_t}\int_{4\pi} d\hat{\Omega}\vec{n}_e\cdot\nabla\Pi\left[\Psi_m^l\right]}{\int_{4\pi} d\hat{\Omega}\Pi\left[\Psi_m^l\right]} - \kappa. \end{aligned} \tag{A.5}$$

First, the SYW face closure is evaluated at the exact solution, Ψ_m^∞, and ϕ^∞:

$$\begin{aligned} C_{F,SYW}\left[\Psi_m^\infty\right](\phi^*,\phi^\infty) &= \left([\![\phi^*]\!],[\![\hat{\kappa}_{SYW}(\Psi_m^\infty)\phi^\infty]\!]\right), \\ \hat{\kappa}_{SYW}(\Psi_m^\infty) &= \underbrace{\frac{\frac{\phi^\infty}{4\pi}\int\limits_{\vec{n}_e\cdot\hat{\Omega}>0} d\hat{\Omega}\left|\vec{n}_e\cdot\hat{\Omega}\right|}{\phi^\infty}}_{1/4} - \kappa = \frac{1}{4} - \kappa, \\ C_{F,SYW}\left[\Psi_m^\infty\right](\phi^*,\phi^\infty) &= \left([\![\phi^*]\!],[\![\left(\frac{1}{4}-\kappa\right)\phi^\infty]\!]\right). \end{aligned} \tag{A.6}$$

As κ can be pulled out of the difference operator and using $\phi^\infty = \text{const} \rightarrow [\![\phi^\infty]\!] = 0$, it follows:

$$C_{F,SYW}\left[\Psi_m^\infty\right](\phi^*,\phi^\infty) = 0. \tag{A.7}$$

Now, we linearize Eq. A.5 around the exact solution:

$$\begin{aligned} C_{F,SYW}\left[\Psi_m^\infty+\epsilon_m^l\right](\phi^*,\phi^\infty+e^{l+1/2}) &= \left([\![\phi^*]\!],[\![\hat{\kappa}_{SYW}(\Psi_m^\infty+\epsilon_m^l)\left(\phi_E+e^{l+1/2}\right)]\!]\right), \\ \hat{\kappa}_{SYW}(\Psi_m^\infty+\epsilon_m^l) &= \frac{\frac{\phi^\infty}{4}+\Pi\left[Y^{out,l}\right]}{\phi^\infty+\Pi\left[E^l\right]} \\ &+ \frac{1}{2}\frac{\frac{1}{3\Sigma_t}\vec{n}_e\cdot\nabla\Pi\left[E^l\right]}{\phi^\infty+\Pi\left[E^l\right]} \\ &- \kappa. \end{aligned} \tag{A.8}$$

Applying Eq. A.1 leads to:

$$\begin{aligned} & C_{F,SYW}\left[\Psi_m^{\infty}+\epsilon^{l+1/2}\right](\phi^*,\phi^{\infty}+e^{l+1/2}) \\ \approx\ & \left(\llbracket\phi^*\rrbracket,\llbracket\frac{\phi^{\infty}}{4}+\frac{e^{l+1/2}}{4}+\Pi\left[Y^{out,l}\right]-\frac{1}{4}\Pi\left[E^l\right]\rrbracket\right) \\ +\ & \left(\llbracket\phi^*\rrbracket,\llbracket\frac{1}{6\Sigma_t}\vec{n}_e\cdot\nabla\Pi\left[E^l\right]\rrbracket\right) \\ -\ & \kappa\left(\llbracket\phi^*\rrbracket,\llbracket e^{l+1/2}\rrbracket\right)-\kappa\left(\llbracket\phi^*\rrbracket,\llbracket\phi^{\infty}\rrbracket\right). \end{aligned} \tag{A.9}$$

Noting again that $\llbracket\phi^{\infty}\rrbracket=0$ yields the final result:

$$\begin{aligned} C_{F,SYW}\left[\Psi_m^{\infty}+\epsilon_m^l\right](\phi^*,\phi^{\infty}+e^{l+1/2}) \approx & \left(\llbracket\phi^*\rrbracket,\llbracket\frac{e^{l+1/2}}{4}+\Pi\left[Y^{out,l}\right]-\frac{1}{4}\Pi\left[E^l\right]\rrbracket\right) \\ & +\left(\llbracket\phi^*\rrbracket,\llbracket\frac{1}{6\Sigma_t}\vec{n}_e\cdot\nabla\Pi\left[E^l\right]\rrbracket\right) \\ & -\kappa\left(\llbracket\phi^*\rrbracket,\llbracket e^{l+1/2}\rrbracket\right). \end{aligned} \tag{A.10}$$

Appendix A.3. Linearization of the pNDA Face Closure

The pNDA closure is given by:

$$\begin{aligned} C_F\left[\Psi_m^l\right](\phi^*,\phi^{l+1/2}) &= \left(\llbracket\phi^*\rrbracket,\llbracket\hat{\kappa}_{pNDA}(\Psi_m^l)\phi^{l+1/2}\rrbracket\right), \\ \hat{\kappa}_{pNDA}(\Psi_m^l) &= \frac{\left[\begin{array}{l}\int\limits_{\vec{n}_e\cdot\vec{\Omega}>0} d\vec{\Omega}\left|\vec{n}_e\cdot\vec{\Omega}\right|\Pi\left[\Psi_m^l\right]-\frac{1}{4}\left\{\!\!\left\{\int_{4\pi}d\vec{\Omega}\Pi\left[\Psi_m^l\right]\right\}\!\!\right\} \\ \quad+\vec{n}\vec{n}_e\llbracket\frac{1}{2}\kappa\int_{4\pi}d\vec{\Omega}\Pi\left[\Psi_m^l\right]-\frac{1}{4}D\int_{4\pi}d\vec{\Omega}\vec{n}_e\cdot\nabla\Pi\left[\Psi_m^l\right]\rrbracket\end{array}\right]}{\int_{4\pi}d\vec{\Omega}\Pi\left[\Psi_m^l\right]}. \end{aligned} \tag{A.11}$$

First, the the pNDA face closure is evaluated using the exact solution Ψ_m^∞, and ϕ^∞:

$$\begin{aligned} C_F\left[\Psi_m^\infty\right](\phi^*,\phi^\infty) &= (\llbracket\phi^*\rrbracket, \llbracket\hat{\kappa}_{pNDA}(\Psi_m^\infty)\phi^\infty\rrbracket) \\ \hat{\kappa}_{pNDA}(\Psi_m^\infty) &= \frac{\left[\begin{array}{l}\int\limits_{\vec{n}_e\cdot\vec{\Omega}>0} d\vec{\Omega}\left|\vec{n}_e\cdot\vec{\Omega}\right|\Pi\left[\Psi_m^\infty\right] - \frac{1}{4}\{\!\{\Pi\left[\Phi^\infty\right]\}\!\} \\ \quad + \vec{n}\vec{n}_e\llbracket\frac{1}{2}\kappa\Pi\left[\Phi^\infty\right] - \frac{1}{4}D\vec{n}_e\cdot\nabla\Pi\left[\Phi^\infty\right]\rrbracket\end{array}\right]}{\Pi\left[\Phi^\infty\right]}. \\ &= \frac{\int\limits_{\vec{n}_e\cdot\vec{\Omega}>0} d\vec{\Omega}\left|\vec{n}_e\cdot\vec{\Omega}\right|\Pi\left[\Phi^\infty\right] - \frac{1}{4}\Pi\left[\Psi_m^\infty\right] + \vec{n}\vec{n}_e\llbracket\frac{1}{2}\kappa\Pi\left[\Phi^\infty\right]\rrbracket}{\Pi\left[\Phi^\infty\right]}. \end{aligned} \tag{A.12}$$

Simplifying Eq. A.12 using the properties of Φ^∞ and ϕ^∞ leads to:

$$\begin{aligned} C_F\left[\Psi_m^\infty\right](\phi^*,\phi^\infty) &= \left(\llbracket\phi^*\rrbracket, \llbracket\frac{\phi^\infty}{4}\rrbracket - \underbrace{\frac{1}{4}\llbracket\{\!\{\phi^\infty\}\!\}\rrbracket}_{=0} + \underbrace{\llbracket\frac{1}{2}\vec{n}\vec{n}_e\llbracket\kappa\phi^\infty\rrbracket\rrbracket}_{-\llbracket\kappa\phi^\infty\rrbracket}\right) \\ &= \left(\llbracket\phi^*\rrbracket, \left(\frac{1}{4}-\kappa\right)\underbrace{\llbracket\phi^\infty\rrbracket}_{=0}\right) = 0. \end{aligned} \tag{A.13}$$

Evaluation of the pNDA closure at the iterates Ψ_m^l and $\phi^{l+1/2}$ leads to:

$$\begin{aligned} &C_{F,pNDA}\left[\Psi_m^\infty + \epsilon_m^l\right](\phi^*,\phi^\infty + e^{l+1/2}) = \\ &= \left(\llbracket\phi^*\rrbracket, \left[\left[\left[\frac{\left[\begin{array}{l}\int\limits_{\vec{n}_e\cdot\vec{\Omega}>0} d\vec{\Omega}\left|\vec{n}_e\cdot\vec{\Omega}\right|\Pi\left[\Psi_m^\infty+\epsilon_m^l\right] - \frac{1}{4}\{\!\{\int_{4\pi} d\vec{\Omega}\Pi\left[\Psi_m^\infty+\epsilon_m^l\right]\}\!\} \\ \quad + \vec{n}\vec{n}_e\llbracket\frac{1}{2}\kappa\int_{4\pi} d\vec{\Omega}\Pi\left[\Psi_m^\infty+\epsilon_m^l\right] - \frac{1}{4}D\int_{4\pi} d\vec{\Omega}\vec{n}_e\nabla\Pi\left[\epsilon_m^l\right]\rrbracket\end{array}\right]}{\int_{4\pi} d\vec{\Omega}\Pi\left[\Psi_m^\infty+\epsilon_m^l\right]}\left(\phi^\infty + e^{l+1/2}\right)\right]\right]\right]\right) \\ &= \left(\llbracket\phi^*\rrbracket, \left[\left[\left[\frac{\left[\begin{array}{l}\frac{\phi^\infty}{4} + \Pi\left[Y^{out,l}\right] - \frac{1}{4}\{\!\{\phi^\infty\}\!\} - \frac{1}{4}\{\!\{\Pi\left[E^l\right]\}\!\} \\ \quad + \vec{n}\vec{n}_e\llbracket\frac{1}{2}\kappa(\phi^\infty + \Pi\left[E^l\right]) - \frac{1}{4}D\vec{n}_e\nabla\Pi\left[E^l\right]\rrbracket\end{array}\right]}{\phi^\infty + \Pi\left[E^l\right]}\left(\phi^\infty + e^{l+1/2}\right)\right]\right]\right]\right) \end{aligned} \tag{A.14}$$

Since the exact solution is constant in space, it follows that $\{\!\{\phi^\infty\}\!\} = \phi^\infty$. Therefore, Eq. A.13 becomes:

$$
\begin{aligned}
C_{F,pNDA} \quad & \left[\Psi_m^\infty + \epsilon^l\right](\phi^*, \phi^\infty + e^{l+1/2}) = \\
= \quad & \left([\![\phi^*]\!], \left[\left[\left[\frac{\left[\begin{array}{c}\Pi\left[Y^{out,l}\right] - \frac{1}{4}\{\!\{\Pi\left[E^l\right]\}\!\} + \frac{1}{2}\kappa\vec{n}\vec{n}_e[\![\phi^\infty]\!] \\ + \vec{n}\vec{n}_e[\![\frac{1}{2}\kappa\Pi\left[E^l\right] - \frac{1}{4}D\vec{n}_e\nabla\Pi\left[E^l\right]]\!]\end{array}\right]}{\phi^\infty + \Pi\left[E^l\right]} \left(\phi^\infty + e^{l+1/2}\right) \right]\right]\right) \\
= \quad & \left([\![\phi^*]\!], \left[\left[\left[\frac{\left[\begin{array}{c}\Pi\left[Y^{out,l}\right] - \frac{1}{4}\{\!\{\Pi\left[E^l\right]\}\!\} \\ + \vec{n}\vec{n}_e[\![\frac{1}{2}\kappa\Pi\left[E^l\right] - \frac{1}{4}D\vec{n}_e\nabla\Pi\left[E^l\right]]\!]\end{array}\right]}{\phi^\infty + \Pi\left[E^l\right]} \left(\phi^\infty + e^{l+1/2}\right) \right]\right]\right)
\end{aligned}
\tag{A.15}
$$

Comparing Eq. A.15 with Eq. A.1, we recognize that $x^\infty = 0$ and therefore the linearization of Eq. A.15 simply is:

$$
\begin{aligned}
& C_{F,NDA}\left[\Psi_m^\infty + \epsilon_m^l\right](\phi^*, \phi^\infty + e^{l+1/2}) \\
\approx \quad & \left([\![\phi^*]\!], [\![\Pi\left[Y^{out,l}\right] - \frac{1}{4}\{\!\{\Pi\left[E^l\right]\}\!\} + \vec{n}\vec{n}_e[\![\frac{1}{2}\kappa\Pi\left[E^l\right] - \frac{1}{4}D\vec{n}_e\nabla\Pi\left[E^l\right]]\!]\!] \right) \\
= \quad & \left([\![\phi^*]\!], [\![\Pi\left[Y^{out,l}\right] - \kappa\Pi\left[E^l\right] + \frac{1}{2}D\vec{n}_e\nabla\Pi\left[E^l\right]]\!] \right).
\end{aligned}
\tag{A.16}
$$

Appendix B. Fourier Analysis of pNDA-AD method for Constant-Constant Approximation in Slab Geometry

Appendix B.1. The Transport System

The transport system is given by:

$$
\mu_n \frac{\partial \Psi_n^{l+1/2}}{\partial x} + \sigma_t \Psi_n^{l+1/2}(\vec{r}) = \frac{\sigma_s}{2}\phi^l. \tag{B.1}
$$

Applying the step-method discretization leads to the following set of equations:

$$
\begin{aligned}
\frac{\mu_n}{\sigma_t \Delta x}\left(\Psi_{n,i+1/2}^{l+1/2} - \Psi_{n,i-1/2}^{l+1/2}\right) + \Psi_{n,i}^{l+1/2} &= \frac{c}{2}\phi_i^l \\
\text{if } \mu_n > 0: \;\; \Psi_{n,i+1/2}^{l+1/2} = \Psi_{n,i}^{l+1/2}, \;\; & \Psi_{n,i-1/2}^{l+1/2} = \Psi_{n,i-1}^{l+1/2} \\
\text{if } \mu_n < 0: \;\; \Psi_{n,i+1/2}^{l+1/2} = \Psi_{n,i+1}^{l+1/2}, \;\; & \Psi_{n,i-1/2}^{l+1/2} = \Psi_{n,i}^{l+1/2}.
\end{aligned}
\tag{B.2}
$$

where Δx is the mesh spacing, c is the scattering ratio, l is the iteration index, and i is the spatial element index. Eliminating edge quantities leads to:

$$\begin{aligned} \text{if } \mu_n > 0: \ & \frac{|\mu_n|}{\sigma_t \Delta x}\left(\Psi_{n,i}^{l+1/2} - \Psi_{n,i-1}^{l+1/2}\right) + \Psi_{n,i}^{l+1/2} = \frac{c}{2}\phi_i^l \\ \text{if } \mu_n < 0: \ & \frac{|\mu_n|}{\sigma_t \Delta x}\left(\Psi_{n,i}^{l+1/2} - \Psi_{n,i+1}^{l+1/2}\right) + \Psi_{n,i}^{l+1/2} = \frac{c}{2}\phi_i^l. \end{aligned} \tag{B.3}$$

The exact solution $(\Psi_{n,i}^{\infty}, \phi_i^{\infty})$ satisfies the equation above, so substitution and subtraction leads to:

$$\begin{aligned} \text{if } \mu_n > 0: \ & \frac{|\mu_n|}{\sigma_t \Delta x}\left(\epsilon_{n,i}^{l+1/2} - \epsilon_{n,i-1}^{l+1/2}\right) + \epsilon_{n,i}^{l+1/2} = \frac{c}{2}e_i^l \\ \text{if } \mu_n < 0: \ & \frac{|\mu_n|}{\sigma_t \Delta x}\left(\epsilon_{n,i}^{l+1/2} - \epsilon_{n,i+1}^{l+1/2}\right) + \epsilon_{n,i}^{l+1/2} = \frac{c}{2}e_i^l. \end{aligned} \tag{B.4}$$

Since the problem is periodic, the values of ϵ at the grid points are given by:

$$\begin{aligned} \epsilon_{n,i}^{l+1/2} &= \epsilon_{n,i}^{l+1/2} \\ \epsilon_{n,i-1}^{l+1/2} &= \epsilon_{n,i}^{l+1/2} \exp(-j\lambda\sigma_t\Delta x) \\ \epsilon_{n,i+1}^{l+1/2} &= \epsilon_{n,i}^{l+1/2} \exp(j\lambda\sigma_t\Delta x), \end{aligned} \tag{B.5}$$

where $j = \sqrt{-1}$ and λ is the wave number. Finally, we can solve for $\epsilon_{n,i}^{l+1/2}$:

$$\epsilon_{n,i}^{l+1/2} = \begin{cases} \frac{c}{2}\frac{e_i^l}{1+\frac{|\mu_n|}{\sigma_t\Delta x}(1-\exp(-j\lambda\sigma_t\Delta x))} & \text{if } \mu_n > 0; \\ \frac{c}{2}\frac{e_i^l}{1+\frac{|\mu_n|}{\sigma_t\Delta x}(1-\exp(j\lambda\sigma_t\Delta x))} & \text{if } \mu_n < 0. \end{cases} \tag{B.6}$$

Appendix B.2. Diffusion System - AD

The diffusion system is given by:

$$\sigma_t(1-c)\Delta x\phi_i^{l+1} + \left(\frac{J_{i\to i+1}^{l+1/2}}{\Phi_i^{l+1/2}}\phi_i^{l+1} - \frac{J_{i+1\to i}^{l+1/2}}{\Phi_{i+1}^{l+1/2}}\phi_{i+1}^{l+1}\right) + \left(\frac{J_{i\to i-1}^{l+1/2}}{\Phi_i^{l+1/2}}\phi_i^{l+1} - \frac{J_{i-1\to i}^{l+1/2}}{\Phi_{i-1}^{l+1/2}}\phi_{i-1}^{l+1}\right) = 0, \tag{B.7}$$

where $J_{i\to i'}$is the partial current from element i to i'. Evaluating Eq. B.7 using the exact solution and subtracting it from the same equation evaluated

at the current iterative solution gives:

$$\sigma_t(1-c)\Delta x e_i^{l+1} + \left(\frac{Y_{i\to i+1}^{l+1/2} + J_{i\to i+1}^{\infty}}{E_i^{l+1/2}+\phi_i^{\infty}}\left(e_i^{l+1}+\phi_i^{\infty}\right) - \frac{J_{i\to i+1}^{\infty}}{\phi_i^{\infty}}\phi_i^{\infty}\right) - \left(\frac{Y_{i+1\to i}^{l+1/2} + J_{i+1\to i}^{\infty}}{E_{i+1}^{l+1/2}+\phi_{\infty}^{l+1/2}}(e_{i+1}^{l+1}+\phi_{i+1}^{\infty}) - \frac{J_{i+1\to i}^{\infty}}{\phi_{i+1}^{\infty}}\phi_{i+1}^{\infty}\right) \left(\frac{Y_{i\to i-1}^{l+1/2} + J_{i\to i-1}^{\infty}}{E_i^{l+1/2}+\phi_i^{\infty}}\left(e_i^{l+1}+\phi_i^{\infty}\right) - \frac{J_{i\to i-1}^{\infty}}{\phi_i^{\infty}}\phi_i^{\infty}\right) - \left(\frac{Y_{i-1\to i}^{l+1/2} + J_{i-1\to i}^{\infty}}{E_{i-1}^{l+1/2}+\phi_{\infty}^{l-1/2}}(e_{i-1}^{l+1}+\phi_{i-1}^{\infty}) - \frac{J_{i-1\to i}^{\infty}}{\phi_{i-1}^{\infty}}\phi_{i-1}^{\infty}\right) = 0 \quad \text{(B.8)}$$

Noting that all $J^{\infty}=0$ leads to:

$$\sigma_t(1-c)\Delta x e_i^{l+1} + \frac{Y_{i\to i+1}^{l+1/2}}{E_i^{l+1/2}+\phi_i^{\infty}}\left(e_i^{l+1}+\phi_i^{\infty}\right) - \frac{Y_{i+1\to i}^{l+1/2}}{E_{i+1}^{l+1/2}+\phi_{\infty}^{l+1/2}}(e_{i+1}^{l+1}+\phi_{i+1}^{\infty}) \frac{Y_{i\to i-1}^{l+1/2}}{E_i^{l+1/2}+\phi_i^{\infty}}\left(e_i^{l+1}+\phi_i^{\infty}\right) - \frac{Y_{i-1\to i}^{l+1/2}}{E_{i-1}^{l+1/2}+\phi_{\infty}^{l-1/2}}(e_{i-1}^{l+1}+\phi_{i-1}^{\infty}) = 0 \quad \text{(B.9)}$$

Linearization of Eq. B.9 yields:

$$\sigma_t(1-c)\Delta x e_i^{l+1} + Y_{i\to i+1}^{l+1/2} - Y_{i+1\to i}^{l+1/2} + Y_{i\to i-1}^{l+1/2} - Y_{i-1\to i}^{l+1/2} = 0 \quad \text{(B.10)}$$

Using the definition of the partial currents we replace the $Y^{l+1/2}$ by $\epsilon^{l+1/2}$:

$$\sigma_t(1-c)\Delta x e_i^{l+1} + \sum_{n:\mu_n>0} w_n\left|\mu_n\right|\epsilon_{n,i}^{l+1/2} - \sum_{n:\mu_n<0} w_n\left|\mu_n\right|\epsilon_{n,i+1}^{l+1/2} + \sum_{n:\mu_n<0} w_n\left|\mu_n\right|\epsilon_{n,i}^{l+1/2} - \sum_{n:\mu_n>0} w_n\left|\mu_n\right|\epsilon_{n,i-1}^{l+1/2} = 0 \quad \text{(B.11)}$$

Finally, using periodicity of the error the following expression is obtained:

$$\sigma_t(1-c)\Delta x e_i^{l+1} + \sum_{n:\mu_n>0} w_n\left|\mu_n\right|\epsilon_{n,i}^{l+1/2} - \sum_{n:\mu_n<0} w_n\left|\mu_n\right|\epsilon_{n,i}^{l+1/2}\exp(j\lambda\sigma_t\Delta x) + \sum_{n:\mu_n<0} w_n\left|\mu_n\right|\epsilon_{n,i}^{l+1/2} - \sum_{n:\mu_n>0} w_n\left|\mu_n\right|\epsilon_{n,i}^{l+1/2}\exp(-j\lambda\sigma_t\Delta x) = 0 \quad \text{(B.12)}$$

Substituting Eq. B.6 into Eq. B.12 and solving for e_i^{l+1} leads to

$$\begin{aligned} e_i^{l+1} = e_i^l \frac{1}{\Delta x \sigma_t (c-1)} \Bigg[& \sum_{n:\mu_n>0} w_n \left|\mu_n\right| \frac{c}{2} \frac{\sigma_t \Delta x}{|\mu_n|} \frac{1}{\frac{\sigma_t \Delta x}{|\mu_n|} + 1 - \exp(-j\lambda\sigma_t\Delta x)} \\ & - \sum_{n:\mu_n<0} w_n \left|\mu_n\right| \frac{c}{2} \frac{\sigma_t \Delta x}{|\mu_n|} \frac{\exp(j\lambda\sigma_t\Delta x)}{\frac{\sigma_t \Delta x}{|\mu_n|} + 1 - \exp(j\lambda\sigma_t\Delta x)} \\ & + \sum_{n:\mu_n<0} w_n \left|\mu_n\right| \frac{c}{2} \frac{\sigma_t \Delta x}{|\mu_n|} \frac{1}{\frac{\sigma_t \Delta x}{|\mu_n|} + 1 - \exp(j\lambda\sigma_t\Delta x)} \\ & - \sum_{n:\mu_n>0} w_n \left|\mu_n\right| \frac{c}{2} \frac{\sigma_t \Delta x}{|\mu_n|} \frac{\exp(-j\lambda\sigma_t\Delta x)}{\frac{\sigma_t \Delta x}{|\mu_n|} + 1 - \exp(-j\lambda\sigma_t\Delta x)} \Bigg] \end{aligned} \tag{B.13}$$

Simplifying this expression finally gives:

$$\begin{aligned} e_i^{l+1} = e_i^l \frac{c}{2(c-1)} \Bigg[& \sum_{n:\mu_n>0} w_n \frac{1 - \exp(-j\lambda\sigma_t\Delta x)}{\frac{\sigma_t \Delta x}{|\mu_n|} + 1 - \exp(-j\lambda\sigma_t\Delta x)} \\ & + \sum_{n:\mu_n<0} w_n \frac{1 - \exp(j\lambda\sigma_t\Delta x)}{\frac{\sigma_t \Delta x}{|\mu_n|} + 1 - \exp(j\lambda\sigma_t\Delta x)} \Bigg]. \end{aligned} \tag{B.14}$$

For small optical thicknesses $\exp(\pm j\lambda\sigma_t\Delta x) \approx 1 \pm j\lambda\sigma_t\Delta x$ and thus:

$$e_i^{l+1} = e_i^l \frac{c}{c-1} \sum_{n:\mu_n>0} w_n \left|\mu_n\right| \frac{\lambda^2}{1+\lambda^2}. \tag{B.15}$$

Since $0 < \lambda < \frac{2\pi}{\sigma_t \Delta x}$, the upper bound of this expressions for $\sigma_t \Delta x \to 0$ goes to infinity. Further the term

$$g(\lambda) = \frac{\lambda^2}{1+\lambda^2}$$

is strictly monotonically increasing and asymptotes to unity for $\lambda \to \infty$. For $\lambda \to \infty$ we therefore have $g(\lambda) \to 1$. Hence, the spectral radius for optically small cells is given by:

$$\rho = \frac{c}{1-c} \sum_{n:\mu_n>0} w_n \left|\mu_n\right|. \tag{B.16}$$

Note that

$$\sum_{n:\mu_n>0} w_n \left|\mu_n\right| \approx \int_0^1 d\mu\mu = \frac{1}{2},$$

and therefore the spectral radius for small optical thicknesses depends only weakly on the quadrature rule and we can write:

$$\rho \approx \frac{1}{2}\frac{c}{1-c}. \tag{B.17}$$

The pNDA-AD method for (constant)/(constant) FEM bases evaluated at the limit of optically small elements becomes unstable for $c > 2/3$.

Appendix C. Bibliography

[1] D. Gaston, C. Newman, G. Hansen, D. Lebrun-Grandie, Moose: A parallel computational framework for coupled systems of nonlinear equations, Nuclear Engineering and Design 239 (2009) 1768 – 1778.

[2] D. Crawford, et al., Experimental capabilities of the transient reactor test (TREAT) facility, in: 1999 ANS Winter Meeting, 1999.

[3] Y. Wang, Nonlinear diffusion acceleration for the multigroup transport equation discretized with sn and continuous fem with rattlesnake, in: International Conference on Mathematics and Computational Methods Applied to Nuclear Science and Engineering, Idaho Falls, ID, 2013.

[4] E. Lewis, W. Miller, Computational Methods of Neutron Transport, ANS, 1993.

[5] J. Willert, H. Park, D. Knoll, A comparison of acceleration methods for solving the neutron transport k-eigenvalue problem, Journal of Computational Physics 274 (2014) 681–694. doi:10.1016/j.jcp.2014.06.044.

[6] R. Alcouffe, Diffusion synthetic acceleration methods for the diamond-differenced discrete-ordinates equations, Nuclear Science and Engineering 64 (1977) 344–355.

[7] E. W. Larsen, Unconditionally stable diffusion-synthetic acceleration methods for the slab geometry discrete ordinates equations. part i: Theory, Nuclear Science and Engineering 82 (1982) 47–63.

[8] M. Adams, W. Martin, Diffusion synthetic acceleration of discontinuous finite element transport iterations, Nuclear Science and Engineering 111 (1992) 145–167.

[9] D. Anistratov, V. Gol'din, Multilevel quasidiffusion methods for solving multigroup transport k-eigenvalue problems in one-dimensional slab geometry, Nuclear Science and Engineering 169 (2011) 111–132.

[10] Y. Chao, Coarse mesh finite difference methods and applications, in: Proceeding Physor 2000, Pittsburgh, PA, 2000.

[11] D. W. Lee, H. Joo, Development of a sn transport code based on discontinuous finite element method and coarse mesh finite difference formulation, in: An International Conference on Mathematics and Computational Methods Applied to Nuclear Science and Engineering, Sun Valley, ID, 2013.

[12] Y. Wang, H. Zhang, R. Martineau, Diffusion acceleration schemes for the self-adjoint angular flux formulation with void treatment, Nuclear Science and Engineering 176 (2014) 201–225.

[13] M. Adams, E. Larsen, Fast iterative methods for discrete-ordinates particle transport calculations, Progress in Nuclear Energy 40 (2002) 3–159.

[14] J. Warsa, W. T.A., J. Morel, Fully consistent diffusion synthetic acceleration of linear discontinuous sn transport discretizations on unstructured tetrahedral meshes, Nuclear Science and Engineering 141 (2002) 236–251.

[15] J. Warsa, W. T.A., J. Morel, Krylov iterative methods and the degraded effectiveness of diffusion synthetic acceleration for multidimensional sn calculations in problems with material discontinuities, Nuclear Science and Engineering 147 (2004) 218–248.

[16] Y. Wang, Adaptive mesh refinement solution techniques for the multigroup sn transport equation using a higher-order discontinuous finite element method, Ph.D. thesis, Texas A&M University, College Station, TX, USA (May 2009).

[17] K. Smith, Nodal method storage reduction by nonlinear iterations, in: Trans. Am. Nucl. Society, Vol. 44, pp. 265-266, 1983.

[18] D. Lee, T. Downar, Y. Kim, Convergence analysis of the nonlinear coarse-mesh finite difference method for one-dimensional fixed-source neutron diffusion problem, Nuclear Science and Engineering 147 (2004) 1–21.

[19] L. Li, K. Smith, B. Forget, Techniques for stabilizing coarse-mesh finite difference (CMFD) in methods of characteristics (MOC), in: MC2015 - Joint International Conference on Mathematics and Computation (M&C), Supercomputing in Nuclear Applications (SNA) and the Monte Carlo (MC) method, Nashville, TN, 2015.

[20] E. W. Larsen, B. W. Kelley, The relationship between the coarse-mesh finite difference and the coarse-mesh diffusion synthetic acceleration methods, Nuclear Science and Engineering 178 (2014) 1–15.

[21] H. Park, D. Knoll, N. C.K., Nonlinear acceleration of transport criticality problems, Nuclear Science and Engineering 172 (2012) 52–65.

[22] S. Schunert, Y. Wang, J. Ortensi, F. Gleicher, M. DeHart, R. Martineau, A high-order nonlinear diffusion acceleration for the s_n equations discretized with the discontinuous fem, in: 2015 ANS Winter Meeting and Nuclear Technology Expo, 2015.

[23] S. Schunert, Y. Wang, J. Ortensi, F. Gleicher, M. DeHart, R. Martineau, A high-order nonlinear diffusion acceleration for the sn equations discretized with the discontinuous fem: Fourier analysis, in: 2015 ANS Winter Meeting and Nuclear Technology Expo, 2015.

[24] D. Valougeorgis, M. William, E. Larsen, Stability analysis of synthetic acceleration methods with anisotropic scattering, Nuclear Science and Engineering 99 (1988) 91–98.

[25] S. Schunert, H. Hammer, J. Lou, Y. Wang, J. Ortensi, F. Gleicher, B. Baker, M. DeHart, R. Martineau, Using directional diffusion coefficients for nonlinear diffusion acceleration of the first order SN equations in near-void regions, in: 2016 ANS Winter Meeting and Nuclear Technology Expo, 2016.

[26] R. Sanchez, C. Rabiti, Y. Wang, Nonlinear acceleration of a continuous finite element discretization of the self-adjoint angular flux form of the transport equation, Nuclear Science and Engineering 175 (2013) 213–226.

[27] H. van Emden, U. Meier Yang, Boomeramg: A parallel algebraic multigrid solver and preconditioner, Applied Numerical Mathematics 41 (2002) 155–177.

[28] S. Schunert, Y. Wang, J. Ortensi, F. Gleicher, B. Baker, M. DeHart, R. Martineau, On the degradation of the effectiveness of nonlinear diffusion acceleration with parallel block jacobi splitting, in: 2016 ANS Summer Meeting, 2016.

[29] I. Wolfram Research, Mathematica: Version 10.3, https://www.wolfram.com/mathematica/ (2015).

[30] Y. Azmy, J. Morel, T. Wareing, Effect of material homogeneity on the performance of dsa for even-parity SN methods, in: International Conference on Mathematics and Computation, Reactor Physics and Environmental Analysis in Nuclear Applications, 1999.

[31] Benchmark on deterministic transport calculations without spatial homogenisation, Tech. Rep. 5420, Nuclear Energy Agency (2005).